A&A 664, A107 (2022)
https://doi.org/10.1051/0004-6361/202243806

Astronomy & Astrophysics

Near-ultraviolet to visible spectroscopy of the Themis and Polana-Eulalia complex families

E. Tatsumi (巽瑛理)[1,2,3], F. Tinaut-Ruano[1,2], J. de León[1,2], M. Popescu[4], and J. Licandro[1,2]

[1] Instituto de Astrofísica de Canarias (IAC), University of La Laguna, La Laguna, Tenerife, Spain
e-mail: etatsumi@iac.es
[2] Department of Astrophysics, University of La Laguna, La Laguna, Tenerife, Spain
[3] Department of Earth and Planetary Science, The University of Tokyo, Bunkyo, Tokyo, Japan
[4] Astronomical Institute of Romanian Academy, Bucharest, Romania

Received 18 April 2022 / Accepted 12 May 2022

ABSTRACT

Context. Spectrophotometric data of asteroids obtained in the 1980s showed that there are large variations in their near-ultraviolet (NUV) reflectance spectra. Reflectance spectra at NUV wavelengths are important because they help detect the presence of hydrated minerals and organics on the asteroid surfaces. However, the NUV wavelength region has not been fully investigated yet using spectroscopic data.
Aims. The aim of our study is to obtain the near-ultraviolet to visible (NUV-VIS, 0.35–0.95 μm) reflectance spectra of primitive asteroids with a focus on members of the Themis and Polana-Eulalia complex families. This characterization allows us to discuss the origin of two recent sample return mission target asteroids, (162173) Ryugu and (101955) Bennu.
Methods. We obtain low-resolution visible spectra of target asteroids down to 0.35 μm using the telescopes located at the Roque de los Muchachos Observatory (La Palma, Spain) and revisit spectroscopic data that have already been published. Using new spectroscopic and already published spectrophotometric and spectroscopic data, we study the characteristics of the NUV-VIS reflectance spectra of primitive asteroids, focusing on data of the Themis family and the Polana-Eulalia family complex. Finally, we compare the NUV characteristics of these families with (162173) Ryugu and (101955) Bennu. In this work, we also study systematic effects due to the use of the five commonly used stars in Landolt's catalog as solar analogs to obtain the asteroid reflectance in the NUV wavelength range. We compare the spectra of five G-stars in Landolt's catalog with the spectrum of the well-studied solar analog Hyades 64, also observed on the same nights.
Results. We find that many widely used Landolt's G-type stars are not solar analogs in the NUV wavelength spectral region and thus are not suitable for obtaining the reflectance spectra of asteroids. We also find that, even though the Themis family and the Polana-Eulalia family complex show a similar blueness at visible wavelengths, the NUV absorption of the Themis family is much deeper than that of the Polana-Eulalia family complex. We did not find significant differences between the New Polana and Eulalia families in terms of the NUV-VIS slope. (162173) Ryugu's and (101955) Bennu's spectral characteristics in the NUV-VIS overlaps with those of the Polana-Eulalia family complex which implies that it is the most likely origin of these two near-Earth asteroids.

Key words. minor planets, asteroids: general – techniques: imaging spectroscopy – minor planets, asteroids: individual: Ryugu – methods: observational

1. Introduction

Photometric studies of asteroids in the NUV (0.35–0.50 μm) started in the 1950s using photomultiplier tubes with UBV broadband filters (e.g., Groeneveld & Kuiper 1954; Wood & Kuiper 1963) mainly because the photoelectric response of CsSb detectors used at that time was better at those wavelengths. These studies found that asteroids showed variation in *U-B* and/or *B-V* colors. The first asteroid large survey with wide wavelength coverage from the NUV to near infrared was done using 24 narrowband filters (the so-called 24 color asteroid survey, Chapman & Gaffey 1979; McFadden et al. 1984). The spectral reflectance curves were found to be indicative of silicate-rich (S) compositions to carbonaceous-rich (C) compositions, which were related to certain classes of meteorites (McCord & Gaffey 1974). Around the same time, a study in the NUV region using the UBV system was expanded to a larger number of objects and found that it is possible to distinguish S, C, and 'unclassified' groups by UBV color only (Zellner et al. 1975; Bowell & Lumme 1979). The significance of the NUV was understood in terms of broad ultraviolet charge exchange absorptions due to transition metal ions, principally Fe^{2+} in a silicate lattice (Gaffey 1976). Shortly after that, Zellner et al. (1985) expanded the wavelength range to 0.34–1.04 μm using an indium-gallium-arsenide-phosphide (InGaAsP) photomultiplier of high quantum efficiency and eight filters, known as the Eight Color Asteroid Survey (ECAS).

The introduction of charge-coupled devices (CCDs) greatly increased the ability to obtain higher wavelength resolution spectroscopy of fainter objects. However, CCDs' quantum efficiency decreases drastically in the NUV. This led most of the spectroscopic surveys, such as Small Main Belt Asteroid Spectroscopic Survey (SMASS) I, II, and Small Solar System Objects Spectroscopic Survey (S^3OS^2), to stay in the visible (VIS) wavelength range, in other words, at wavelengths >0.45 μm (Xu et al. 1995; Bus & Binzel 2002b,a; Lazzaro et al. 2004). In this study, we expand the wavelength range down to 0.35 μm to study the diagnostics in the NUV with a focus on carbonaceous asteroids.

Among carbonaceous asteroids, those with a negative visible spectral slope (i.e., spectrally blue) are gaining a great deal of attention because of several ongoing and planned missions to these types of objects, such as NASA OSIRIS-REx, JAXA Hayabusa2, and DESTINY+ (Lauretta et al. 2019; Watanabe et al. 2019; Sarli et al. 2018). The relation between the target asteroids of these missions: (101955) Bennu, (162173) Ryugu, and (3200) Phaeton, respectively, and their precursor bodies in the main asteroid belt, is an important question still to be addressed. We focus on two large, low-albedo asteroid families, the Themis family and the Polana-Eulalia complex family, in which the largest members are spectrally blue (Xu et al. 1995; Bus & Binzel 2002b; de León et al. 2016; Tatsumi et al., in prep.). The Polana-Eulalia family complex is located in the inner main belt and is considered to be the most likely origin of both Ryugu and Bennu (Campins et al. 2010a, 2013; Bottke et al. 2015). This was the starting point of our PRIMitive Asteroids Spectroscopic Survey (PRIMASS; Pinilla-Alonso et al. 2021), in which we focused on acquiring visible and near-infrared spectra (and NUV spectra to a minor extent) of primitive, carbonaceous-like asteroids in the main belt. We gave particular attention to members of collisional families and/or dynamical groups (de León et al. 2016; Pinilla-Alonso et al. 2016; Morate et al. 2016, 2018, 2019; De Prá et al. 2018, 2020; Arredondo et al. 2020, 2021).

In the 1980s, the great variation in reflectance in the NUV was pointed out (e.g., Tholen 1984). Based on the NUV and near infrared observations, Feierberg et al. (1985) suggested that this variation is due to the correlation between NUV absorption and the 3-μm band depth, which is mainly caused by the presence of hydroxyl in phyllosilicates. Moreover, Hiroi et al. (1993, 1996) find a similar correlation in hydrated meteorites (CM, CI) through heating experiments. More recently, it was pointed out that the carbon or magnetite formed by the space weathering process on the asteroid surfaces might also affect the NUV behavior (Izawa et al. 2019; Hendrix & Vilas 2019). Thus, the NUV region can be potentially used as a diagnostic for finding hydrated minerals or carbon compounds, although the possibility has not been fully investigated so far. This study opens a new door to ground-based spectroscopy in the NUV region.

In this work, we investigate the NUV-VIS spectra of these families in the frame of the PRIMASS survey, and we discuss their composition to further study the role of phyllosilicates and explain the presence of NUV absorption. In addition, we discuss the importance of using well-characterized solar analog stars in the NUV region, and the problems we have found with many of the most commonly used stars in the planetary science community. The paper is organized as follows: spectroscopic observations (including solar analogs), and data reduction are described in Sect. 2; spectral slope calculations, solar analog correction, and comparison with spectrophotometry from the previous survey ECAS are presented in Sect. 3; finally, we discuss the results and summarize conclusions in Sects. 4 and 5, respectively.

2. Observations and data reduction

2.1. Asteroid observations at TNG

The NUV-VIS spectra at the 3.58-m Telescopio Nazionale Galileo (TNG), located at the Roque de Los Muchachos Observatory (ORM) on the island of La Palma (Spain), were obtained with the Device Optimized for the LOw RESolution (DOLORES) spectrograph. The instrument is equipped with a 2048 × 2048 pixels detector and a 0.25″ pixel^{-1} plate scale, which yields a 8.6′ × 8.6′ field of view. The low-resolution LR-B (blue) and LR-R (red) grisms were used, covering the 0.34– 0.80 μm and the 0.45–1.01 μm spectral ranges with a dispersion of 2.5 and 2.6 Å pixel^{-1}, respectively. We used 1.5″ or 2.0″ slits oriented at the parallactic angle and set the tracking of the telescope to the asteroids' proper motion. The observations on the nights of February 6, 7, and 8, 2012 were done in the framework of B-type asteroid study by de León et al. (2012) in which they analyzed the spectral behavior of a sample of 45 B-type asteroids in the near-infrared. The idea was to expand that study to the NUV region, observing those B-types and also some members of the Themis collisional family. Observations on the nights of October 30, and 31 and November 1, 11, and 12, 2010, were originally published by de León et al. (2016), in which they studied the visible spectra of members of the Polana-Eulalia family complex and presented NUV spectra for some of them. For this paper, we downloaded the corresponding raw spectra (of the asteroids and the solar analog stars) from the TNG archive[1] and did a new data reduction to account for identified problems in the behavior of the solar analogs in the NUV which we explain in Sect. 3.1. To enlarge our NUV spectral sample, we did a further search in the TNG archive. We looked for any asteroid spectra obtained with the LR-B grism that were observed only on nights when the solar analog star Hyades 64 was also observed (see Sect. 2.3). The enlarged sample includes asteroids from other collisional families, rocky asteroids (non-carbonaceous), and even a couple of Trojans. This dataset includes the observations by Cellino et al. (2020), but we applied the different data reduction procedure. It is important to note here that, although we do not use some of these spectra for our scientific discussions, we have decided to keep them in the study as they are a valuable and trustworthy dataset of NUV-VIS asteroidal data that could be useful for future studies. Table A.1 shows the observation conditions of the asteroids, including the date and UTC start time, the apparent visual magnitude of the asteroid at the time of observation (m_V), the exposure time for each of the grisms (LR-B and LR-R), the airmass (AM), and the phase angle.

2.2. Observation of (162173) Ryugu at GTC

On December 6, 2020, the Japanese spacecraft Hayabusa2 successfully returned samples from the carbonaceous-like asteroid (162173) Ryugu to Earth. When the spacecraft dropped the sample container, Ryugu was approaching Earth, which made observations from the ground very favorable. We therefore obtained low-resolution NUV-VIS spectra of Ryugu using the 10.4-m Gran Telescopio Canarias (GTC), also located at ORM, under program GTC75-20B. The spectra were obtained using the Optical System for Imaging and Low Resolution Integrated Spectroscopy (OSIRIS) camera spectrograph (Cepa et al. 2000; Cepa 2010) installed at the GTC. The optical spectrometer OSIRIS is equipped with two 2048 × 4096 pixel detectors and a total unvignetted field of view of 7.8′ × 7.8′. We used the 1.2″ slit and the R300B grism with a dispersion of 5 Å pixel^{-1}, which covers 0.36–0.85 μm. The observations were conducted by orienting the slit along the parallactic angle to minimize the effects of atmospheric differential refraction and the telescope tracking was set to the asteroid's proper motion. A series of three spectra was obtained, with an offset of 10″ in the slit direction in between individual spectra. We applied the same procedure to the stars. Observational details are shown in Table 1. To obtain the asteroid's reflectance spectrum, we observed solar analog

[1] http://archives.ia2.inaf.it/tng/

Table 1. Observations conducted at GTC.

Object	Date and time (UTC)	m_V	Airmass	Exposure time (s)
(162173) Ryugu	2020-10-27 00:34:34	16.9	1.26–1.30	3×300
SA 93-101	2020-10-27 00:48:45	9.7	1.135	3×1
SA 98-978	2020-10-27 03:31:44	10.6	1.35	3×1

Table 2. Landolt's G-stars observed in this study.

Solar analog	Other designation	RA (J2000)	Dec (J2000)	m_V	Sp. type	[Fe/H]
Hyades 64	HD 28099	04 26 40.12	+16 44 48.9	8.1	G2+V	0.06 dex
SA 93-101	HD 11532	01 53 18.37	+00 22 23.3	9.7	G8III/IV	−0.3 dex
SA 98-978	HD 292561	06 51 33.7	−00 11 31.5	10.6	F8	−1.2 dex
SA 102-1081	BD+00 2717	10 57 04.0	−00 13 12.9	9.9	G5IV	0.2 dex
SA 107-684	HD 139287	15 37 18.1	−00 09 49.7	8.4	G2/3V	−0.2 dex
SA 112-1333	BD-00 4074	20 43 12.0	+00 26 13.1	9.9	F8	−0.9 dex

References. The metallicity is from Miller et al. (2015); Datson et al. (2015); Xiang et al. (2019).

stars SA 93-101 and SA 98-978 at a similar AM. In the following section, we further describe the importance of properly selecting these stars.

2.3. Star observations

In asteroid spectroscopy, we need to remove the solar contribution from the observed asteroid spectra. To do this, the solar analog stars instead of the Sun are commonly used because the Sun is too bright for telescope observations. Historically, planetary scientists have broadly used G-type stars as solar analogs as they are known to be spectrally very close to the Sun in visible wavelengths (it should be noted that, after new observations, some of them were recently reclassified from G to F type, see Table 2). Several G-type stars listed in Landolt (1973, 1983, 1992) are commonly used as solar analogs based on their photometric colors and temperatures. However, as a consequence of our interest in the NUV region, we have discovered that many of these widely used stars are either not well-characterized below 0.45–0.5 μm or do not have a spectral behavior in the NUV region similar to that of the Sun. It is widely acknowledged that it is hard to find a solar analog in the NUV wavelength range (Hardorp 1978). This is because small variations in the CN and CH abundances and the metallicity of G-type stars introduce significantly large differences in the flux around 0.387 and 0.43 μm, and a photon flux below 0.5 μm, respectively (Hardorp 1978; Porto de Mello et al. 2014). To minimize this problem, previous photometric surveys avoided the use of solar analogs. They instead observed well-characterized standard stars and computed their relative flux to the Sun (Chapman & Salisbury 1973; DeMeo & Carry 2013) or they used only the well-characterized solar analogs by Hardorp (1980) to define the zero point of the color system (Tedesco et al. 1982).

Another way to avoid the problem is to use solar analogs that are well characterized in the NUV. Hardorp (1978, 1980) found several solar spectral analogs in the NUV: Hyades 64 (HD 28099), Hyades 106 (HD 29461), Hyades 142 (HD 30246), 16 Cyg B (HD 186427), HD 44594, and HD 191854. Later, Neckel (1986) confirmed Hyades 64, 16 Cyg B (HD 186427), and HD 44594 are very close to the Sun in UBV color and Farnham et al. (2000) confirmed that Hyades 64 (HD 28099), Hyades 106 (HD 29461), 16 Cyg B (HD 186427), and HD 191854 behave similar to the Sun when observed with the HB narrowband filter designed for comet observations. Among them, Hyades 64 (HD 28099) and 16 Cyg B (HD 186427) are commonly acknowledged as the best-matched solar analogs down to the NUV. ECAS adopted the mean color of four stars from Hardorp's solar analogs as the zero point of their photometric system (Tedesco et al. 1982). This means that ECAS's photometric colors have carefully taken into account the NUV color of the Sun. Thus, the photometric surveys (24 color survey and ECAS) are trustworthy data for studying NUV reflectance.

Hyades 64 was observed every night with the TNG under the same conditions as those described in Sect. 2.1. We also observed five commonly used Landolt (1973) G-type stars (Table 2) and checked whether they are spectrally good solar analogs in the NUV.

Additionally, we collected data on these stars from previous observations done by authors who used different telescopes, such as the 2.56-m Nordic Optical Telescope (NOT) and the 2.54-m Isaac Newton Telescope (INT) at ORM (Table 2). In the case of the INT, we obtained the spectra using the Intermediate Dispersion Spectrograph (IDS) together with the low resolution grism R150V and a wide slit (3″). At NOT, we used the Alhambra Faint Object Spectrograph (ALFOSC) and the low resolution grism #4, with a 5″ slit. The date and time of observation, the AM, and the telescope used for each solar analog are shown in Table 3. We use Hyades 64 as a reference for a good solar analog in the NUV. The subsequent analysis of the other stars compared to Hyades 64 is presented in Sect. 3.1.

2.4. Data reduction

We applied the standard procedures to the obtained images, such as bias subtraction, flat-field correction, wavelength calibration, and extraction of one-dimensional spectra from two-dimensional images. The wavelength calibration and extraction of spectra were conducted using "apall" and "identify" functions in the Image Reduction and Analysis Facility (IRAF; Tody 1986). Atmospheric extinction correction was applied using the standard extinction coefficients for ORM[2].

[2] http://www.ing.iac.es/Astronomy/observing/manuals/ps/tech_notes/tn031.pdf

Table 3. Landolt's G-type star and Hyades 64 observed by various telescopes.

Date time (UTC)	Solar analog	AM	Telescope
2008-10-03 21:05:23	SA 112-1333	1.13	NOT
2008-10-04 01:41:50	SA 93-101	1.15	NOT
2008-10-04 20:21:03	SA 112-1333	1.15	NOT
2008-10-05 06:10:58	SA 98-978	1.17	NOT
2009-10-05 06:22:34	Hyades 64	1.11	NOT
2010-10-30 19:54:02	SA 112-1333	1.15	TNG
2010-10-31 02:15:51	SA 93-101	1.27	TNG
2010-10-31 04:04:37	Hyades 64	1.06	TNG
2010-10-31 21:10:45	SA 112-1333	1.30	TNG
2010-10-31 21:55:27	SA 112-1333	1.48	TNG
2010-11-01 01:29:42	Hyades 64	1.09	TNG
2010-11-10 23:41:42	SA 93-101	1.13	TNG
2010-11-11 02:22:51	Hyades 64	1.02	TNG
2010-11-11 02:28:01	Hyades 64	1.02	TNG
2010-11-11 20:08:03	SA 112-1333	1.24	TNG
2010-11-12 00:19:54	SA 93-101	1.15	TNG
2010-11-12 02:44:53	Hyades 64	1.03	TNG
2010-11-12 23:53:50	SA 93-101	1.14	TNG
2010-11-13 02:48:12	Hyades 64	1.03	TNG
2012-02-06 22:42:38	Hyades 64	1.18	TNG
2012-02-06 22:55:48	SA 98-978	1.14	TNG
2012-02-07 01:26:41	SA 102-1081	1.25	TNG
2012-02-07 05:38:18	SA 107-684	1.33	TNG
2012-02-07 22:32:38	SA 98-978	1.34	TNG
2012-02-07 22:47:49	Hyades 64	1.21	TNG
2012-02-08 01:57:09	SA 102-1081	1.21	TNG
2012-02-08 05:45:35	SA 107-684	1.29	TNG
2022-01-13 00:20:10	Hyades 64	1.18	INT
2022-01-13 01:15:26	SA 98-978	1.17	INT
2022-01-13 04:52:26	SA 102-1081	1.15	INT
2022-01-13 22:11:52	SA 93-101	1.48	INT
2022-01-13 23:37:10	SA 98-978	1.17	INT
2022-01-14 03:54:30	SA 102-1081	1.16	INT

The asteroids' reflectance spectra were obtained by dividing the observed asteroid flux by a spectrum of a solar analog. As we explain in Sect. 3.1, we used Hyades 64 for the TNG observations. When both the LR-B and LR-R spectra were available, we joined the blue and red parts of the spectra using the common wavelength interval of 0.6–0.7 μm. For asteroids (6698) and (13100), which were observed on two different nights, we averaged the two spectra together. Finally, the spectra were binned every 3 Å. All the observed spectra are shown in Fig. A.1. We also show smoothed spectra obtained by running the median filter using a window of ∼30 nm for a better visualization. We describe the procedure to obtain the reflectance spectra of Ryugu in Sect. 3.4.

3. Analyses and results

3.1. Solar analogs

In this sub-section, we provide a description of our study of the spectral behavior of the observed solar analogs in the NUV. As we mentioned in Sect. 2.3, we consider Hyades 64 to be a reference star for the NUV. For each night of observation, we therefore divided the spectra of Landolt's stars by that of

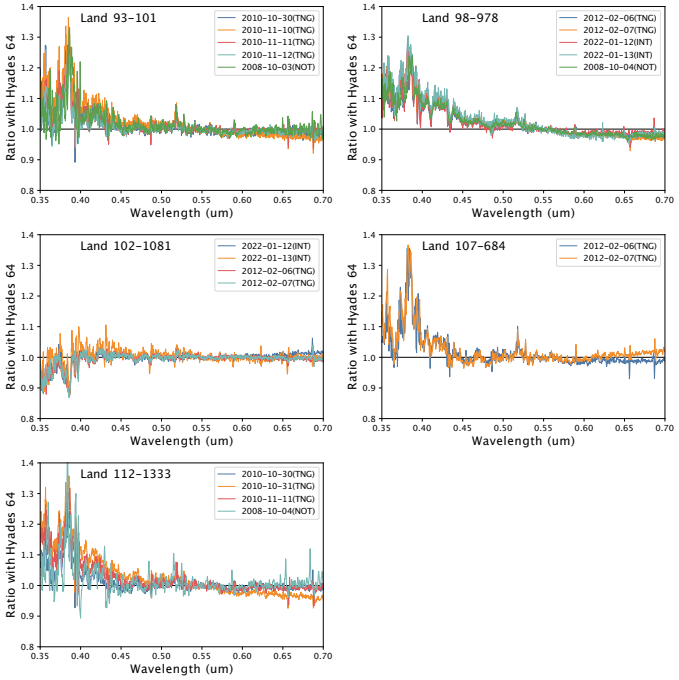

Fig. 1. Ratio between Landolt's stars and Hyades 64. The spectra were normalized to unity at 0.55 μm.

Hyades 64 and normalized the obtained ratio at 0.55 μm in order to show their spectral variation in the NUV (Fig. 1). The results are consistent even when using different telescopes and instruments. The first remarkable result is that the spectra of Landolt's stars at wavelengths above 0.55 μm are very similar to those of the Sun. On the other hand, below 0.55 μm the spectral differences are very important. We observe a strong excess in the CN band for SA 93-101, SA 98-978, SA 107-684, and SA 112-1333, and a deficiency for SA 102-1081. The spectral slopes, especially in the NUV, are also different from that of Hyades 64, with differences in slope in visible wavelengths (0.55–0.85 μm) being within the standard deviation. The turning up or down of reflectance in the NUV is likely due to the difference in metallicity of the stars. The metallicity, for example, can be characterized by the iron abundance [Fe/H]. Even when the spectral type is similar to that of our Sun, if the iron abundance is less than the Sun's (<0 dex), the flux in UV can be significantly higher (Buser & Kurucz 1992). We should note that if one uses SA 93-101, SA 98-978, SA 107-684, or SA 112-1333 as a solar analog to derive the reflectance spectra of asteroids, the flux excess will artificially create a fake absorption in the NUV, in other words, a drop in reflectance. Among the stars analyzed here, the one that presents the closest spectral slope to that of the Sun in NUV-VIS is SA 102-1081, although it still has a significant deficiency in its NUV flux compared with the Sun.

Our results show that only one out of the five commonly used solar analog stars studied here can be used to get reflectance spectra of asteroids in the NUV even though there is still up to a 10% difference in the shortest wavelength. This should be noted when interpreting results on previous studies using Landolt's solar analogs in the NUV. A good example of this case is presented in Sect. 4.2, where we revisit the results obtained in de León et al. (2016) for the Polana-Eulalia complex family. We remark that these stars can be used to obtain reflectance spectra of asteroids in the visible (0.5–0.9 μm) and the near-infrared (0.8–2.4 μm). Spectral slopes for these Landolt's stars were

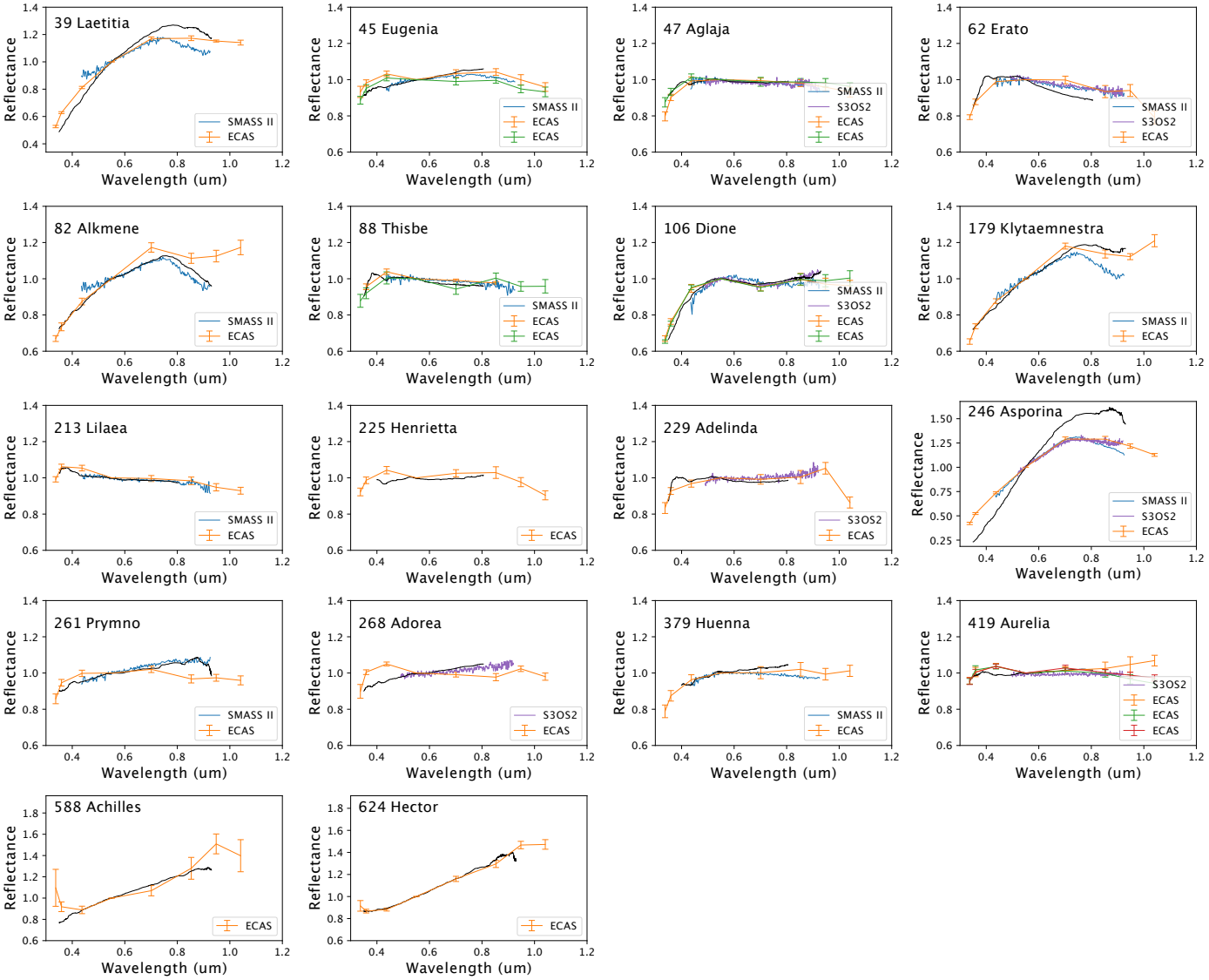

Fig. 2. Asteroids observed in this study compared with ECAS (orange, green, and red), SMASS II (blue), and S^3OS^2 (purple). The TNG spectra are shown with black lines. The spectra are normalized to unity at 0.55 μm.

investigated precisely and statistically by Marsset et al. (2020), and they found them to be consistent with the Sun with an uncertainty of 4.2% μm^{-1}.

Thus, in this study, we use Hyades 64 as the solar analog to derive asteroid reflectance spectra down to the NUV. We will devote some effort to finding more solar analogs in the NUV region for the further study of reflectance spectroscopy.

3.2. Comparison of our observations with ECAS

Observations of spectral reflectance in the wavelength range between 0.34 and 1.04 μm by ECAS greatly advanced our understanding of the compositional distribution of asteroids (Tholen 1984; Zellner et al. 1985). Zellner et al. (1985) obtained more than 900 photometric reflectance spectra using eight broadband filters covering this wavelength interval: *s* (0.34 μm), *u* (0.36 μm), *b* (0.44 μm), *v* (0.55 μm), *w* (0.70 μm), *x* (0.85 μm), *p* (0.95 μm), and *z* (1.04 μm). They treated carefully the NUV reflectance photometric spectra using solar analogs that were well characterized in the NUV. A total of 18 out of the 67 asteroids presented in this paper were also observed in the frame of the ECAS survey. Thus, we can make a comparison and validate our methodology. Figure 2 shows their obtained spectra with the TNG, together with the spectrophotometric observations by ECAS (Zellner et al. 1985), as well as SMASS II (Bus & Binzel 2002b) and S^3OS^2 (Lazzaro et al. 2004). We note that spectra from SMASS II and S^3OS^2 cover only visible wavelengths.

In general, we obtained consistent results compared with ECAS spectrophotometry in NUV-VIS, except maybe for asteroids (246) Asporina, (268) Adorea, and (588) Achilles. Some of our targets show in their NUV spectra a clear turn-off point, in other words, a position in wavelength where the slope changes its value drastically. That is case for asteroids (47) Aglaja, (62) Erato, (88) Thisbe, and (229) Adelinda, which have a turn-off point in the NUV at around 0.4 μm. These turning points were not clearly observed in their ECAS spectra because of the low wavelength resolution. We also note that some ECAS spectra have an excess in the *b* filter that our spectra do not show. This may be because the zero point of the ECAS color index was defined by four solar analogs and they might have some systematic error (Tedesco et al. 1982). The central wavelength of

the b filter (0.44 μm) is located very close to the CH absorption band. Thus, this band needs to be carefully interpreted. Our spectra show good agreement with other surveys at visible wavelengths considering the range of spectral variations between surveys. Only (246) Asporina shows much redder spectra than the other three surveys. Differences in the phase angle (α) could be invoked to explain the observed difference in spectral slope (phase reddening): our spectrum was obtained at a phase angle of ~22°, while the SMASS II and S^{3}OS^2 spectra were obtained at a phase angle of ~8°. This corresponds to a change in spectral slope of 1%/10^{3}Å/° for 8° < α < 22°, computed in the range 0.48–0.72 μm, following the same procedure as that described in Luu & Jewitt (1990). They obtained a change of 0.18%/10^{3}Å/° for 0° < α < 40° for a sample of near-Earth and main belt asteroids. Our change in slope is five times larger than the one in Luu & Jewitt (1990), suggesting phase reddening cannot be the sole explanation for the difference in spectral slope. In addition, the ECAS data are in good agreement with both SMASS II and S^{3}OS^2 spectra, but were obtained at a phase angle of ~16.6°.

3.3. NUV-VIS spectra of Themis, Polana, and Eulalia families

Members of the Themis collisional family in our sample were identified using the list from Nesvorný et al. (2015), available in the Planetary Data System (PDS). As explained in Sect. 2.1, members of the Polana-Eulalia family complex were taken from de León et al. (2016). In that paper, the authors searched for spectral differences between the members of the Eulalia family and the so-called "New Polana" family, identified by Walsh et al. (2013). We also collected spectrophotometric data from ECAS of asteroids belonging to the Themis family and the Polana-Eulalia family complex. We computed the NUV and VIS slopes by linear least square fitting for the wavelength ranges 0.36–0.55 μm and 0.55–0.85 μm, respectively. For the ECAS photometric spectra, the errors in the slope were calculated from 100 samples created by the bootstrap method according to the deviation given for each ECAS filter. The list of Themis, Polana, and Eulalia family members with TNG spectra and ECAS photometric data are shown in Tables 4 and 5, respectively. The asteroid (5924) Teruo was initially classified as belonging to the Nysa-Polana family by Nesvorný et al. (2015), but it was classified as belonging to neither the New Polana nor Eulalia families by Walsh et al. (2013). Thus, because of its low albedo, we decided to list (5924) Teruo as an uncategorized Polana-Eulalia family member in Table 4. We also include in Table 4 other dark, carbonaceous-like asteroids and our taxonomical classification (see Sect. A.1). Other information we included are the Bus and Tholen taxonomies (Bus & Binzel 2002a; Tholen 1984) from ECAS, SMASS II and S^{3}OS^2 spectra, albedo and diameter from the AKARI survey (Usui et al. 2012), and the NUV and VIS slopes.

3.4. Computing a reliable NUV-VIS spectrum of (162173) Ryugu

We followed the same data reduction procedure for the GTC spectra as that described in Sect. 2.4 for the TNG up to the extraction of one-dimensional spectra of both Ryugu and the G-type stars SA 93-101 and SA 98-978. The R300B grism at OSIRIS-GTC provides a full spectrum from 0.36 to 0.85 μm. Solar analog star Hyades 64 could not be observed because it is too bright for a 10-m class telescope (m_V = 8.1) and it would saturate even with sub-second exposures. As concluded in Sect. 3.1, the observed Landolt stars showed a significant variation from a solar-like spectral behavior in the NUV. To correct for such variation in SA 93-101 and SA 98-978, we calculated the Ryugu's reflectance spectrum, $R_{\rm Ryugu}$, as follows:

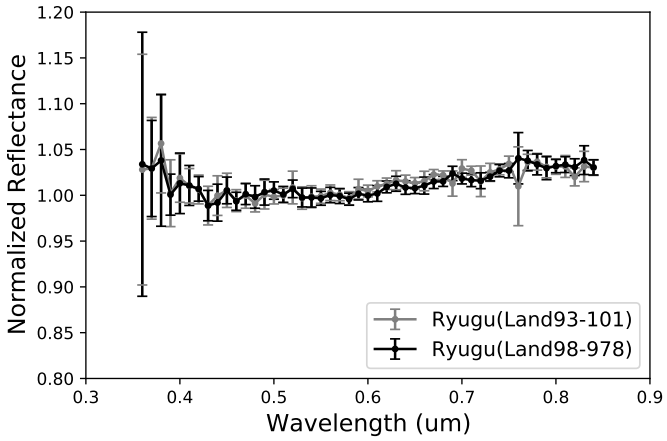

Fig. 3. (162173) Ryugu observed with the GTC on 27 October 2020. We derived the asteroid's NUV-VIS reflectance spectra against two Landolt stars (SA 93-101 and SA 98-978) corrected based on the observations of Hyades 64 with the TNG.

$$R_{\rm Ryugu} = \frac{F^{\rm GTC}_{\rm Ryugu}}{F^{\rm GTC}_{\rm SA}} \frac{F^{\rm TNG}_{\rm SA}}{F^{\rm TNG}_{\rm H64}}, \quad (1)$$

where $F^{\rm GTC}_{\rm Ryugu}$ is the Ryugu spectrum from the GTC, $F^{\rm GTC}_{\rm SA}$ is the solar analog spectra from the GTC (with SA being SA 93-101 and SA 98-978), $F^{\rm TNG}_{\rm SA}$ is the solar analog spectra from the TNG, and $F^{\rm TNG}_{\rm H64}$ is the Hyades 64 spectrum from the TNG. The ratio $F^{\rm TNG}_{\rm SA}/F^{\rm TNG}_{\rm H64}$ for SA 93-101 was obtained on three different nights, while for SA 98-978 it was obtained on two different nights (see Table 3). We used an average of all the ratios for each solar analog star. The final reflectance spectra of Ryugu was binned by 10 Å (Fig. 3). The two spectra obtained against two Landolt's stars show good agreement, exhibiting a flat or possibly upturned slope in the NUV region. These spectra are also consistent with what was observed by Hayabusa2 (Sugita et al. 2019; Tatsumi et al. 2020).

4. Discussion

In this section, we discuss the NUV-VIS characteristics of the Themis family and Polana-Eulalia family complex and the two sample-return mission targets, (162173) Ryugu and (101955) Bennu. We compare the members of the Themis, New Polana, and Eulalia families in the NUV-VIS space obtained from our observations and ECAS data (Table 5). The NUV and VIS spectral slopes were computed from 0.36 to 0.55 μm and from 0.55 to 0.85 μm, respectively. To evaluate the the NUV absorption, we used the difference of spectral slopes between NUV and VIS: $A_{\rm NUV} = S_{\rm NUV} - S_{\rm VIS}$.

4.1. Themis family

The Themis collisional family consists of about 2400 to 4300 members and is located in the outer main belt at 3.1 au (Nesvorný et al. 2005; Spoto et al. 2015). The age of this collisional family can be estimated based on the relation between objects' semi-major axis and size among the family members, which was mainly configured by thermal forces via the Yarkovsky effect

Table 4. Members of the New Polana, Eulalia, and Themis families, as well as other dark, carbonaceous-like asteroids observed with the TNG.

ID	Name	Taxonomy (this study)	Taxonomy Bus	Taxonomy Tholen	Albedo	Diameter (km)	NUV slope (μm^{-1})	VIS slope (μm^{-1})
New Polana family								
2026	Cottrell	C/P/F	–	–	0.088 ± 0.009	13.2 ± 0.6	–	0.08 ± 0.02
3485	Barucci	F	–	–	0.075 ± 0.003	14.7 ± 0.3	0.01 ± 0.02	0.01 ± 0.01
5158	Ogarev	F	–	–	0.067 ± 0.012	7.8 ± 0.7	0.05 ± 0.03	−0.01 ± 0.01
6578	Zapesotskij	F	–	–	0.061 ± 0.005 (#)	7.9 ± 0.1 (#)	0.07 ± 0.03	−0.04 ± 0.01
6661	Ikemura	F	–	–	0.087 ±0.004	10.9 ± 0.2	−0.30 ± 0.02	−0.09 ± 0.01
6769	Brokoff	F	–	–	0.052 ±0.006	12.8±0.7	−0.38 ± 0.03	0.02 ± 0.02
8424	Toshitsumita	C	–	–	0.165 ± 0.03 (#)	5.2 ± 0.1 (#)	0.45 ± 0.02	0.19 ± 0.01
33804	1999WL4	C	–	–	0.072 ± 0.011 (#)	5.4 ± 0.1 (#)	0.47 ± 0.02	0.04 ± 0.01
Eulalia family								
6142	Tantawi	F	–	–	0.092 ± 0.034 (#)	9.2 ± 1.7 (#)	−0.55 ± 0.03	−0.26 ± 0.02
6698	Malhotra	F	–	–	0.097 ± 0.011	8.3 ± 0.5	−0.06 ± 0.03	−0.07 ± 0.02
6840	1995WW5	F	–	–	0.043 ± 0.008 (#)	8.6 ± 0.1 (#)	−0.06 ± 0.03	−0.10 ± 0.01
9052	Uhland	F	–	–	0.047 ± 0.004	10.2 ± 0.4	−0.07 ± 0.02	−0.11 ± 0.01
25490	Kevinkelly	B	–	–	0.043 ± 0.007	8.1 ± 0.7	−0.10 ± 0.03	−0.03 ± 0.01
49833	1999XB84	F	–	–	0.064 ± 0.004 (#)	4.3 ± 0.1 (#)	0.11 ± 0.03	−0.09 ± 0.01
Polana-Eulalia Family (Uncategorized)								
5924	Teruo	F	–	–	0.054 ± 0.004	14.8 ± 0.5	−0.12 ± 0.02	0.00 ± 0.01
Themis family								
62	Erato	B (†)	Ch	BU	0.091 ± 0.002	79 ± 1	0.30 ± 0.02	−0.44 ± 0.01
268	Adorea	P/C (†)	X (*)	FC	0.046 ± 0.001	136 ± 2	0.41 ± 0.02	0.22 ± 0.01
379	Huenna	C (†)	C	B	0.075 ± 0.002	82 ± 1	–	0.15 ± 0.01
461	Saskia	C/B (†)	X	FCX	0.069 ± 0.005	43 ± 1	0.36 ± 0.02	0.01 ± 0.01
468	Lina	C/B/G/F (†)	Xk (*)	DPF	0.059 ± 0.002	60 ± 1	–	0.07 ± 0.02
555	Norma	B/F (†)	B	–	0.101 ± 0.004	32 ± 1	–	−0.23 ± 0.01
936	Kunigunde	B/F (†)	B (*)	B (*)	0.124 ± 0.007	38 ± 1	–	−0.21 ± 0.01
954	Li	C/G (†)	Cb (*)	FCX	0.068 ± 0.002	53 ± 1	–	0.14 ± 0.01
Other dark asteroids								
45	Eugenia	P/C	C	FC	0.056 ± 0.002	184 ± 4	0.33 ± 0.01	0.28 ± 0.01
47	Aglaja	B (†)	C	B	0.060 ± 0.004	147 ± 2	0.29 ± 0.01	−0.03 ± 0.01
88	Thisbe	B (†)	B	CF	0.071 ± 0.002	196 ± 3	0.00 ± 0.02	−0.13 ± 0.01
106	Dione	G	Cgh	G	0.084 ± 0.003	153 ± 2	1.53 ± 0.02	−0.07 ± 0.01
175	Andromache	C/B	Cg	C	0.093 ± 0.004	96 ± 2	0.51 ± 0.01	−0.09 ± 0.01
207	Hedda	C	Ch	C	0.047 ± 0.002	64 ± 1	0.68 ± 0.02	−0.09 ± 0.01
213	Lilaea	F (†)	B	F	0.107 ± 0.003	76 ± 1	−0.29 ± 0.01	−0.06 ± 0.01
225	Henrietta	B/F/C (†)	–	F	0.051 ± 0.002	108 ± 2	0.03 ± 0.02	0.06 ± 0.01
229	Adelinda	B/F (†)	Cb (*)	BCU	0.034 ± 0.001	109 ± 1	0.08 ± 0.02	−0.03 ± 0.01
419	Aurelia	F (†)	Cb	F	0.051 ± 0.002	122 ± 2	0.00 ± 0.02	0.11 ± 0.01
426	Hippo	C/B/G/F (†)	X (*)	F	0.052 ± 0.002	121 ± 2	–	0.06 ± 0.01
588	Achilles	T	–	DU	0.035±0.002	133±3	1.13 ± 0.02	0.85 ± 0.01
624	Hector	D	–	D	0.034 ± 0.001	231 ± 4	0.75 ± 0.02	1.10 ± 0.01
747	Winchester	P/C (†)	C	PC	0.052 ± 0.002	170 ± 3	0.52 ± 0.02	0.34 ± 0.01
919	Ilsebill	C/G	C	–	0.048 ± 0.002	33 ± 0.5	1.01 ± 0.02	0.10 ± 0.01
1214	Richilde	P	Xk	–	0.064 ± 0.002	34.9 ± 0.5	0.59 ± 0.02	0.29 ± 0.01
1471	Tornio	P	T	–	0.052 ± 0.002	42 ± 0.6	0.19 ± 0.02	0.68 ± 0.01
1534	Nasi	G	Cgh	–	0.100 ± 0.004	19.5 ± 0.4	1.30 ± 0.02	0.08 ± 0.01
3451	Mentor	P	X	–	0.075 ± 0.005	118 ± 3	0.68 ± 0.02	0.32 ± 0.01

Notes. (*)Spectra from S^3OS^2 (Lazzaro et al. 2004). (#)Albedo and diameter values from the NEOWISE. (†)Classification only using blue spectrum (LR-B). Albedo and diameter without marks are from Usui et al. (2012).

Table 5. Members of the New Polana, Eulalia, and Themis families collected from ECAS.

ID	Name	Taxonomy		Albedo	Diameter	NUV slope	VIS slope
		Bus	Tholen		(km)	(μm^{-1})	(μm^{-1})
New Polana family							
83	Beatrix	X	X	0.080 ± 0.002	87 ± 1	0.43 ± 0.12	0.48 ± 0.11
142	Polana	B	F	0.055 ± 0.002	50 ± 1	−0.12 ± 0.14	−0.15 ± 0.11
335	Roberta	B	FP	0.055 ± 0.002	92 ± 1	−0.16 ± 0.07	0.08 ± 0.08
750	Osker	–	F	0.057 ± 0.003	20.9 ± 0.5	−0.40 ± 0.05	−0.05 ± 0.07
1493	Sigrid	Xc	F	0.048 ± 0.002	25.1 ± 0.4	−0.06 ± 0.13	0.01 ± 0.15
1650	Heckmann	–	F	0.034 ± 0.004	35.2 ± 1.7	−0.31 ± 0.10	−0.11 ± 0.14
1768	Appenzella	C	F	0.047 ± 0.002	18.0 ± 0.4	−0.19 ± 0.21	−0.14 ± 0.14
2081	Sazava	–	F	0.045 ± 0.002	23.5 ± 0.5	−0.33 ± 0.11	0.12 ± 0.15
2279	Barto	–	F	0.059 ± 0.004	14.3 ± 0.4	−0.22 ± 0.09	−0.08 ± 0.06
2809	Vernadskij	B	BFX	0.037 ± 0.005 (#)	12.0 ± 0.1 (#)	0.05 ± 0.18	−0.15 ± 0.18
3123	Dunham	–	F	0.040 ± 0.003 (#)	12. ± 0.1 (#)	−0.13 ± 0.18	−0.22 ± 0.17
Eulalia family							
650	Amalasuntha	–	–	0.035 ± 0.002	19.2 ± 0.4	−0.44 ± 0.81	0.53 ± 0.86
969	Leocadia	–	FXU:	0.045 ± 0.001	19.4 ± 0.2	−0.29 ± 0.19	0.29 ± 0.30
1012	Sarema	–	F	0.037 ± 0.002	23.0 ± 0.5	−0.01 ± 0.16	−0.08 ± 0.15
1076	Viola	C	F	0.032 ± 0.002	26.4 ± 0.6	−0.22 ± 0.14	−0.25 ± 0.21
1740	Paavo Nurmi	–	F	0.046 ± 0.006 (#)	12.8 ± 0.2 (#)	−0.35 ± 0.06	0.02 ± 0.05
2139	Makharadze	–	F	0.045 ± 0.007 (#)	17.2 ± 0.1 (#)	0.05 ± 0.18	−0.04 ± 0.23
2278	Gotz	–	FC	0.040 ± 0.003	12.8 ± 0.4	0.40 ± 0.50	−0.63 ± 0.57
Themis family							
24	Themis	B	C	0.084 ± 0.003	177 ± 2	0.67 ± 0.08	−0.14 ± 0.07
62	Erato	Ch	BU	0.091 ± 0.002	79 ± 1	0.62 ± 0.08	−0.23 ± 0.10
90	Antiope	C	C	0.057 ± 0.003	124 ± 2	0.52 ± 0.08	0.00 ± 0.10
171	Ophelia	C	C	0.080 ± 0.002	105 ± 1	0.53 ± 0.11	−0.05 ± 0.14
222	Lucia	–	BU	0.143 ± 0.004	53 ± 1	0.59 ± 0.11	−0.23 ± 0.13
223	Rosa	Xc (*)	X	0.037 ± 0.002	81 ± 1	0.49 ± 0.13	0.36 ± 0.05
268	Adorea	X (*)	FC	0.046 ± 0.001	136 ± 2	−0.05 ± 0.07	−0.08 ± 0.06
379	Huenna	C	B	0.075 ± 0.002	82 ± 1	0.67 ± 0.13	0.06 ± 0.13
383	Janina	B	B	0.133 ± 0.008	38.3 ± 1.0	0.51 ± 0.13	−0.24 ± 0.11
515	Athalia	Cb	U	0.037 ± 0.003	39.8 ± 1.4	1.65 ± 0.11	0.24 ± 0.14
526	Jena	Ch (*)	B	0.076 ± 0.003	45.2 ± 0.7	0.50 ± 0.08	−0.06 ± 0.07
946	Poesia	–	FU	0.097 ± 0.003	39.6 ± 0.6	0.53 ± 0.10	0.14 ± 0.10
996	Hilaritas	–	B	0.069 ± 0.008	33.7 ± 1.8	0.79 ± 0.67	−0.10 ± 0.12
1445	Konkolya	–	C	0.070 ± 0.004	22.3 ± 0.6	0.46 ± 0.12	0.36 ± 0.20
1576	Fabiola	B (*)	BU	0.100 ± 0.015	26.2 ± 1.8	0.03 ± 0.15	−0.22 ± 0.24
1581	Abanderada	–	BCU	0.061 ± 0.002	36.5 ± 0.6	0.50 ± 0.15	−0.53 ± 0.21
1615	Bardwell	Ch (*)	B	0.064 ± 0.008 (#)	27.8 ± 1.6 (#)	0.52 ± 0.17	−0.07 ± 0.20
1691	Oort	Cb (*)	CU	0.053 ± 0.002	36.4 ± 0.7	0.47 ± 0.14	−0.16 ± 0.08
2405	Welch	–	BCU:	0.038 ± 0.002	26.4 ± 0.6	0.59 ± 0.14	−0.14 ± 0.26

Notes. (*)Spectra from S^3OS^2 (Lazzaro et al. 2004). (#)Albedo and diameter values from the NEOWISE survey (Mainzer et al. 2019). Albedo and diameter without marks are from Usui et al. (2012).

(Farinella & Vokrouhlicky 1999; Bottke Jr et al. 2006). The collisional age of the Themis family was estimated to be 2 Gyr by Marzari et al. (1995) and 2.4–3.8 Gyr by Spoto et al. (2015), which puts it among the oldest families in the main belt.

The diameter of the parent body of the Themis family has been estimated to be 390–450 km (Marzari et al. 1995). The largest asteroid in the Themis family is (24) Themis, with a diameter of 198 km. Free water ice or NH_3-bearing phyllosilicates indicated by a 3.1 μm band have been detected on the surface of Themis (Campins et al. 2010a; Rivkin & Emery 2010). Later, Takir & Emery (2012) confirmed the 3.1 μm band and classified Themis as part of the rounded group, one of the four groups they identified based on the shape of the 3-μm absorption band. Usui et al. (2019) showed an absorption of 10.7% at 2.76 μm associated with OH in hydrated minerals and a broad 3.07 μm absorption of 11.9% from the AKARI data. The density value has been estimated at 1.31 ± 0.62 g cm^{-3} (Vernazza et al. 2021). This density is comparable to the bulk density of CI chondrites, 1.57 g cm^{-3}, and CM chondrites, 2.27 g cm^{-3} (Flynn et al. 2018). Considering only 13% of Themis family members show the 0.7 μm feature (De Prá et al. 2020), the majority of the members might be composed of CI-like material rather than CM-like material. However, we cannot rule out the possibility that two lithologies, CI-like and CM-like, are inside the parent

body of the Themis family and Themis itself, considering that some members have the 0.7-μm band and the peak wavelength of the OH band locates at a rather longer wavelength.

The thermal properties of eight Themis family members were investigated by Licandro et al. (2012). Emissivity spectra from 5–14 μm exhibit a plateau at about 9 to 12 μm for five members. This plateau feature is similar to that of comets and P- and D-type asteroids (Vernazza et al. 2015), but the emissivity strength is smaller for the Themis family (Licandro et al. 2012). This feature may indicate the presence of small grain olivine and/or pyroxene (Emery et al. 2006; Vernazza et al. 2015).

From ECAS, about half of the Themis family members were classified as B types (Zellner et al. 1985). Later taxonomic classification based on complementary spectroscopic works came up with a consistent result, with a mean visible spectral slope $S_{\rm VIS} = -0.02 \pm 0.16$ μm^{-1} , and it was found that ∼13% of the asteroids among the Themis family showed the 0.7-μm band absorption (Mothé-Diniz et al. 2005; De Prá et al. 2020). Our analysis provides a mean VIS slope of $S_{\rm VIS} = -0.04 \pm 0.23$ μm^{-1} and a mean NUV absorption of $A_{\rm NUV} = 0.60 \pm 0.31$ μm^{-1}. Our visible slope is consistent with previous studies.

Even though a significant fraction of the Themis family members have negative visible spectra, their near-infrared spectral slopes tend to be positive and thus they have concave shapes from the visible to the near infrared (Clark et al. 2010; Ziffer et al. 2011; de León et al. 2012; Fornasier et al. 2016).

4.2. Polana-Eulalia family complex

Previous studies found that primitive near-earth asteroids Ryugu and Bennu, targets of the sample return missions Hayabusa2 and OSIRIS-REx, respectively, are almost certainly (>90%) delivered from the inner main belt (Campins et al. 2010b, 2013; Bottke et al. 2015). The Polana-Eulalia family complex is the largest low-albedo family in that region. This family is also known to overlap in proper elements space with an S-type asteroid family, Nysa (Cellino et al. 2001). Moreover, the peculiar spectra of the two biggest asteroids, the E-type (44) Nysa and the M-type (135) Hertha, exhibit the complexity of the Polana-Eulalia-Nysa family complex (Cellino et al. 2001; Dykhuis & Greenberg 2015). Recently, inside of this family complex, Walsh et al. (2013) found the presence of two dynamically separated low-albedo families, called the New Polana and Eulalia families. Bottke et al. (2015) estimated the collisional ages of the New Polana and Eulalia families to be 1400 ± 150 Myr and 830^{+370}_{-100} Myr, respectively. The diameter of the parent body of Eulalia was estimated to be ∼100 km based on the size frequency distribution of the family members, which is consistent with the smoothed particle hydrodynamics simulations (Walsh et al. 2013).

Even though (43962) 1997 EX13 and (14112) 1998QZ25 are dynamically classified as members of the New Polana and the Eulalia families, respectively, they are much brighter (with an albedo of 0.17 and 0.22, respectively) than the rest of the family members and are taxonomically classified as S-complex asteroids (see Table A.2). Thus, we consider them to be outliers and exclude them from the analysis. (8424) Toshitsumita could also be an outlier because of its high albedo of 0.17, although it was taxonomically classified as a C type. We cannot discard the possibility of uncertainty in albedo measurement. Therefore, we still include (8482) Toshitsumita in our analysis as a member of the New Polana family.

Although the asteroid (142) Polana is classified as an F type in the Tholen taxonomy, de León et al. (2016) found a minor fraction of F types among the Polana-Eulalia family complex. On the contrary, using the same TNG data that they used, we found that most asteroids in the Polana-Eulalia family complex are classified as F types (Table 4). The main reason for this discrepancy is the use of solar analog stars. While de León et al. (2016) divided the spectrum of the asteroid by the spectra of each solar analog and then averaged these ratios to get the final reflectance spectrum, we only used Hyades 64, which we knew had a solar-like spectral behavior in the NUV region. Our result is quite consistent with what Tholen (1984) found in the ECAS data, and demonstrates the importance of properly selecting solar analogs for NUV studies. We also found that most members of the Polana-Eulalia family complex have very shallow or no NUV absorption down to 0.35 μm.

Regarding the visible wavelengths, we reached the same conclusion as de León et al. (2016). The authors found similar visible spectral slopes for New Polana and Eulalia family members. We also found that the New Polana members and the Eulalia members cannot be distinguished in the NUV-VIS space, although we found that the NUV part of the spectra is flatter than in de León et al. (2016) by using Hyades 64 as the solar analog. The average VIS slope is $S_{\rm VIS} = -0.00 \pm 0.16$ μm^{-1} for the New Polana family and $S_{\rm VIS} = -0.01 \pm 0.34$ μm^{-1} for the Eulalia family. The average of NUV absorption is $A_{\rm NUV} = -0.06 \pm 0.23$ μm^{-1} for the New Polana family and $A_{\rm NUV} = -0.06 \pm 0.46$ μm^{-1} for the Eulalia family.

Furthermore, the near-infrared spectroscopic investigations of the Polana-Eulalia family complex suggest that both families show a concave shape, with a spectral slope of 6.8 ± 6.8%/μm from 0.9 to 2.2 μm, and that there is no significant difference between the two families (Pinilla-Alonso et al. 2016). Our NUV investigations also consistently come to the same result.

4.3. (162173) Ryugu and (101955) Bennu: Comparison with the Themis, New Polana, and Eulalia families in NUV-VIS

There is a significant difference in the NUV absorption, $A_{\rm NUV}$, between the Themis family and the Polana-Eulalia family complex (Fig. 4, lower panel). Except for three objects, members of the Polana-Eulalia family complex are well separated from members of the Themis family in this space: the Themis family shows higher NUV absorptions than the Polana-Eulalia family complex even though the visible spectral slopes are distributed in a similar range of values. Both the Themis family and the Polana-Eulalia family complex show the trend expanding from redder VIS slopes and less NUV absorption to bluer VIS slopes and more NUV absorption. From the upper panel of Fig. 4, we see no apparent difference between the two families in the albedo versus VIS slope space.

From our observation with the GTC (Fig. 3), Ryugu is classified as an F type rather than as a C type in Tholen's taxonomy. The NUV-VIS reflectance spectrum of Ryugu does not show any significant absorption in the NUV down to 0.36 μm, which is more similar to the characteristics of the Polana-Eulalia complex family than those of the Themis family. Although many spectroscpic observations have been done for Ryugu (see Tatsumi et al. 2020), only Binzel et al. (2001); Vilas (2008), and Perna et al. (2017) reached the reflectance spectra down to the NUV. The spectrum obtained by Binzel et al. (2001) shows a concave shape, which is different from the spectra obtained by the Hayabusa2 spacecraft. This might be because of the high AM condition. The spectra obtained by Vilas (2008) and Perna et al. (2017) show a good agreement with the spacecraft-based observation in the VIS. While Vilas (2008) shows quite flat

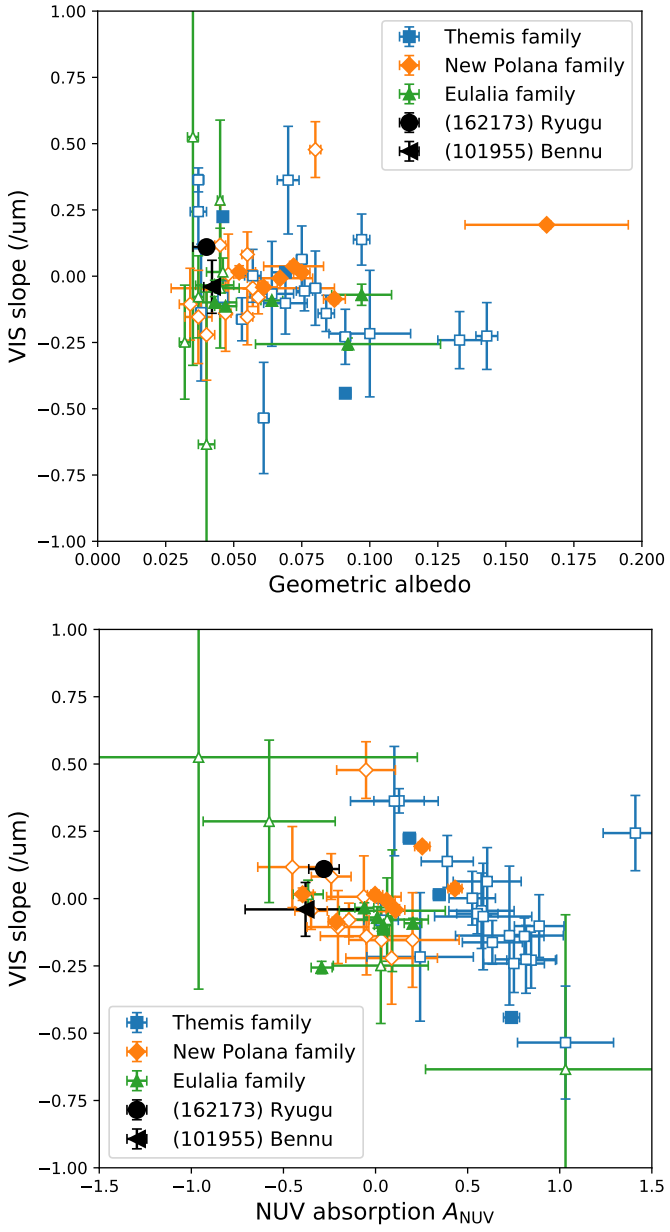

Fig. 4. VIS slope vs. geometric albedo (*upper panel*) and NUV absorption (*lower panel*) for (162173) Ryugu, (101955) Bennu, the Themis family, and the Polana-Eulalia complex family. Filled symbols are observations with the TNG, and open symbols are observations by ECAS (Zellner et al. 1985).

spectra up to 0.39 μm, Perna et al. (2017) shows slight downturns in the shorter wavelengths down to 0.35 μm, which is contrary to what we observed. They used Landolt's stars SA 110-361, SA 113-276, and SA 114-654 as solar analogs, which are not studied in this paper. These stars also need to be evaluated in the NUV before further interpretations can be carried out. Spectral slopes of Ryugu in the NUV and VIS are $S_{\rm NUV} = -0.17 \pm 0.07$ μm^{-1} and $S_{\rm VIS} = 0.11 \pm 0.02$ μm^{-1}, respectively, overlapping with the Polana-Eulalia family complex (Fig. 4). This suggests that Ryugu might originate from the Polana-Eulalia complex, which is located in the inner main asteroid belt where the majority of near-Earth asteroids come from Bottke Jr et al. (2002).

Another target of a sample return mission (OSIRIS-REx), asteroid (101955) Bennu, is also a dark carbonaceous near-Earth asteroid (Lauretta et al. 2019). Bennu was observed using ECAS equivalent color filters from a ground-based telescope (Hergenrother et al. 2013). The visible wavelengths >0.44 μm were found to be consistent with the observations by the OSIRIS-REx Visible and IR Spectrometer (OVIRS) and the multiband camera MapCam on board OSIRIS-REx (Hamilton et al. 2019; DellaGiustina et al. 2020). When we compare Bennu's color with that of the Themis and Polana-Eulalia families, it is found to overlap with the Polana-Eulalia family. Based on the dynamical evolution of Bennu, it was hypothesized that Bennu originated from that of the Polana-Eulalia family complex (Campins et al. 2010b; Bottke et al. 2015). Additionally, the in situ observations by the OSIRIS-REx spacecraft revealed fragments possibly from (4) Vesta on Bennu's surface (DellaGiustina et al. 2021; Tatsumi et al. 2021a). This finding also strongly suggests that Bennu originated in the inner main asteroid belt, at 2.1–2.5 au. Our observations consistently point toward the conclusion that Bennu has similar NUV-VIS characteristics to those of the Polana-Eulalia family complex.

Although both Ryugu and Bennu could originate from the Polana-Eulalia complex family in terms of similarity in the NUV-VIS spectroscopy, the spectra in the 3-μm region of these asteroids are different. While remote-sensing observations by Hayabusa2 of Ryugu showed a sharp OH band centered at 2.72 μm (Kitazato et al. 2019), which was confirmed by the Ryugu sample analysis that showed a sharp and deep OH band centered at 2.71 μm (Yada et al. 2021; Pilorget et al. 2022), the remote-sensing observations by OSIRIS-REx of Bennu showed a broad OH band centered at 2.74 μm (Hamilton et al. 2019). This difference in the central wavelengths and the OH band shapes might reflect the presence of different phyllosilicates, for example, whether they are Mg-bearing or Fe-bearing. Thus, if the two asteroids originate from the same parent body, there should be layers with varying temperature or water-rock conditions inside of the parent body. This will be revealed by the analyses of the samples from both Ryugu and Bennu. Based on the different composition of the exogenic fragments found on both asteroids (Tatsumi et al. 2021b), if they are not from the same parent body, it is more plausible that Bennu comes from the Polana-Eulalia family complex, and that Ryugu comes from a different parent body. It should be noted that the near-Earth environment has a much higher temperature, and more photon and ion irradiation from the Sun than the main asteroid belt, and that this may cause the different reflectance spectra in the NUV region (Hendrix & Vilas 2019). We need further investigations to constrain the origin of F-type asteroids such as Ryugu and Bennu.

4.4. Asteroids with the 0.7-μm absorption bands

The asteroids in our sample that have both the blue and the red parts – (106) Dione, (175) Andromache, (207) Hedda, and (1534) Nasi – show the 0.7-m absorption band. We measured the band depth (in percent) by removing the slope computed between the two local maxima around 0.55 and 0.90 μm (Table 6). These asteroids are classified as G or C types according to Tholen's taxonomy. All the spectra exhibit an absorption in the NUV, with the turning point around 0.52–0.56 μm, which is at longer wavelengths than those of B or F types. The NUV absorptions $A_{\rm NUV}$ of these asteroids are in the range 0.6–1.6 μm^{-1}, while other asteroids without the 0.7-μm band show $A_{\rm NUV} < 0.4$ μm^{-1}. Both the 0.7-μm and the NUV absorptions are caused by the intervalance charge transfer transitions of iron (Vilas 1994). Thus, the abundance of Fe-rich phyllosilicates on asteroids strongly affects the turning point of the NUV absorption. In other words, B or F

Table 6. Depth and central wavelengths for the 0.7-μm absorption bands identified.

ID	Name	Band depth (%)	Central wavelength (μm)
106	Dione	3.2 ± 0.2	0.69
175	Andromache	1.9 ± 1.1	0.67
207	Hedda	3.4 ± 0.7	0.70
1534	Nasi	3.7 ± 1.0	0.72

types may contain less or no Fe-rich phyllosilicates, resulting in a turnoff at shorter wavelengths. The abundance of Fe-rich phyllosilicates can be more precisely assessed by observations in the 3-μm region. This needs further investigation in the future.

5. Summary

We investigated the NUV-VIS reflectance spectra of dark, carbonaceous asteroids, most of them members of the Themis, New Polana, and Eulalia collisional families, but we also included other dark asteroids, rocky, silicate-rich asteroids, and asteroids belonging to other families. To minimize the problems identified when observing in the NUV (0.35–0.50 μm), we observed the asteroids at low AM and used Hyades 64 as a solar analog to obtain the asteroid reflectance spectra. We presented new data obtained with the DOLORES spectrograph at the TNG, using the LR-B (NUV) and the LR-R (VIS) grisms, and also revisited raw spectra previously published by de León et al. (2016). In addition, we searched the TNG archive for other asteroids observed with the same instrumental configuration and with observations of Hyades 64 on the same night. All in all, we collected data for 67 asteroids. A total of 18 out of 67 asteroids were commonly observed at the TNG and by the ECAS survey (Zellner et al. 1985). Their comparison showed a good agreement in the NUV. Their VIS reflectance spectra were also consistent with spectra from other spectroscopic surveys, such as SMASS II (Bus & Binzel 2002b) and S^3OS^2 (Lazzaro et al. 2004). Our observations and collected data confirm the first systematic spectroscopic survey of asteroids in NUV-VIS.

To further study the importance of using proper solar analogs in the NUV region, we observed five of the commonly used Landolt's G-type stars together with Hyades 64 using three different instruments and telescopes: DOLORES@TNG, ALFOSC@NOT, and IDS@INT. The ratios between Landolt's G-type stars and Hyades 64 showed strong variations in the NUV, even though the VIS spectra were consistent with Hyades 64. The CN band exhibited the largest variation among the stars. We find that the metallicity plays a big role in increasing or decreasing the relative flux in the NUV. Among the five studied Landolt's stars, SA 102-1081 was the closest to the solar spectrum, but still showed a depletion in the CN band and the NUV flux. Thus, we need to carefully select a solar analog to derive the NUV-VIS reflectance spectra of asteroids.

The Themis family and the Polana-Eulalia family complex are known to have neutral to blue spectra in visible wavelengths. Our analysis showed that NUV spectra exhibit differences between these families: the Themis family has a deeper NUV absorption than the Polana-Eulalia family complex. Although de León et al. (2016) found that most of the members of the Polana-Eulalia family complex were classified as B type in the Tholen's taxonomy, we find that they are indeed mostly classified as F types, showing a neutral reflectance spectrum from NUV to VIS. This is because de León et al. (2016) used multiple solar analogs, including Landolt's stars, which are not representative of the solar spectrum in the NUV, while we used only Hyades 64, which is known to have very similar spectral behavior in the NUV to that of the Sun. On the other hand, we reached the same conclusion that the sub-families of the complex, the New Polana and the Eulalia families, are not spectrally distinguishable. Thus, they might originate from the same parent body. In an upcoming paper, we study carbonaceous asteroids in the NUV using spectrophotometric surveys (Tatsumi et al., in prep.), suggesting that the NUV absorption observed in asteroids belonging to the Polana, Eulalia, and Themis families might be related to Fe-rich phyllosilicates.

We successfully observed (162173) Ryugu down to 0.36 μm using the GTC in 2020. (162173) Ryugu is the target of the Hayabusa2 sample return mission. We find that the reflectance spectrum of Ryugu shows a flat NUV or a slight increase, which is consistent with spacecraft observations (Sugita et al. 2019; Tatsumi et al. 2020). Thus, Ryugu is classified as an F type rather than a C type by Tholen's taxonomy. Based on our observations, we conclude that Ryugu's spectrum is quite consistent with the reflectance spectra of the Polana-Eulalia family complex. Moreover, the spectrophotometric observation of (101955) Bennu by Hergenrother et al. (2013) suggests that Bennu is also consistent with the Polana-Eulalia family rather than the Themis family.

Acknowledgements. The authors thank to Dr. Pierre Vernazza for the constructive review comments. E.T., F.T.R., J.d.L., and J.L. acknowledge support from the Agencia Estatal de Investigación del Ministerio de Ciencia e Innovación (AEI-MCINN) under grant "Hydrated minerals and organic compounds in primitive asteroids" (PID2020-120464GB-I00/doi:10.13039/501100011033). J.d.L. also acknowledges financial support from the Spanish Ministry of Science and Innovation (MICINN) through the Spanish State Research Agency, under Severo Ochoa Programe 2020-2023 (CEX2019-000920-S). E.T. was also supported by the JSPS core-to-core program, "International Network of Planetary Science". M.P. was supported by the grant of the Romanian National Authority for Scientific Research - UEFISCDI, project No. PN-III-P1-1.1-TE-2019-1504. This research used the facilities of the Italian Center for Astronomical Archive (IA2) operated by INAF at the Astronomical Observatory of Trieste. Based on observations made with the Gran Telescopio Canarias (GTC), installed at the Spanish Observatorio del Roque de los Muchachos of the Instituto de Astrofísica de Canarias, on the island of La Palma. This work is partly based on data obtained with the instrument OSIRIS, built by a Consortium led by the Instituto de Astrofísica de Canarias in collaboration with the Instituto de Astronomía of the Universidad Autónoma de México. OSIRIS was funded by GRANTECAN and the National Plan of Astronomy and Astrophysics of the Spanish Government.

References

Arredondo, A., Lorenzi, V., Pinilla-Alonso, N., et al. 2020, Icarus, 335, 113427
Arredondo, A., Campins, H., Pinilla-Alonso, N., et al. 2021, Icarus, 358, 114210
Binzel, R. P., Harris, A. W., Bus, S. J., & Burbine, T. H. 2001, Icarus, 151, 139
Bottke Jr, W. F., Morbidelli, A., Jedicke, R., et al. 2002, Icarus, 156, 399
Bottke Jr, W. F., Vokrouhlickỳ, D., Rubincam, D. P., & Nesvornỳ, D. 2006, Ann. Rev. Earth Planet. Sci., 34, 157
Bottke, W. F., Vokrouhlickỳ, D., Walsh, K. J., et al. 2015, Icarus, 247, 191
Bowell, E., & Lumme, K. 1979, in Asteroids, eds. T. Gehrels, & M. S. Matthews (Tucon: University of Arizona Press), 132
Bus, S. J., & Binzel, R. P. 2002a, Icarus, 158, 146
Bus, S. J., & Binzel, R. P. 2002b, Icarus, 158, 106
Buser, R., & Kurucz, R. L. 1992, A&A, 264, 557
Campins, H., Hargrove, K., Pinilla-Alonso, N., et al. 2010a, Nature, 464, 1320
Campins, H., Morbidelli, A., Tsiganis, K., et al. 2010b, ApJ, 721, L53
Campins, H., De León, J., Morbidelli, A., et al. 2013, AJ, 146, 26
Cellino, A., Zappalà, V., Doressoundiram, A., et al. 2001, Icarus, 152, 225
Cellino, A., Bendjoya, P., Delbo', M., et al. 2020, A&A, 642, A80
Cepa, J. 2010, Astrophys. Space Sci. Proc., 14, 15
Cepa, J., Aguiar, M., Escalera, V. G., et al. 2000, SPIE Conf. Ser., 4008, 623
Chapman, C. R., & Gaffey, M. J. 1979, in Asteroids, eds. T. Gehrels, & M. S. Matthews (Tucson: University of Arizona Press), 655

Chapman, C. R., & Salisbury, J. W. 1973, Icarus, 19, 507
Clark, B. E., Ziffer, J., Nesvorny, D., et al. 2010, J. Geophys. Res. Planets, 115, E6
Datson, J., Flynn, C., & Portinari, L. 2015, A&A, 574, A124
de León, J., Pinilla-Alonso, N., Campins, H., Licandro, J., & Marzo, G. 2012, Icarus, 218, 196
de León, J., Pinilla-Alonso, N., Delbo, M., et al. 2016, Icarus, 266, 57
DellaGiustina, D., Burke, K., Walsh, K., et al. 2020, Science, 370, eabc3660
DellaGiustina, D. N., Kaplan, H. H., Simon, A. A., et al. 2021, Nat. Astron., 5, 31
DeMeo, F., & Carry, B. 2013, Icarus, 226, 723
De Prá, M. N., Pinilla-Alonso, N., Carvano, J. M., et al. 2018, Icarus, 311, 35
De Prá, M. N., Pinilla-Alonso, N., Carvano, J., et al. 2020, A&A, 643, A102
Dykhuis, M. J., & Greenberg, R. 2015, Icarus, 252, 199
Emery, J. P., Cruikshank, D. P., & Van Cleve, J. 2006, Icarus, 182, 496
Farinella, P., & Vokrouhlicky, D. 1999, Science, 283, 1507
Farnham, T. L., Schleicher, D. G., & A'Hearn, M. F. 2000, Icarus, 147, 180
Feierberg, M. A., Lebofsky, L. A., & Tholen, D. J. 1985, Icarus, 63, 183
Flynn, G. J., Consolmagno, G. J., Brown, P., & Macke, R. J. 2018, Geochemistry, 78, 269
Fornasier, S., Lantz, C., Perna, D., et al. 2016, Icarus, 269, 1
Gaffey, M. J. 1976, J. Geophys. Res., 81, 905
Groeneveld, I., & Kuiper, G. P. 1954, ApJ, 120, 529
Hamilton, V., Simon, A., Christensen, P., et al. 2019, Nat. Astron., 3, 332
Hardorp, J. 1978, A&A, 63, 383
Hardorp, J. 1980, A&A, 88, 334
Hendrix, A. R., & Vilas, F. 2019, Geophys. Res. Lett., 46, 14307
Hergenrother, C. W., Nolan, M. C., Binzel, R. P., et al. 2013, Icarus, 226, 663
Hiroi, T., Pieters, C. M., Zolensky, M. E., & Lipschutz, M. E. 1993, Science, 261, 1016
Hiroi, T., Pieters, C. M., Zolensky, M. E., & Prinz, M. 1996, Lunar Planet. Sci. Conf., 27, 551
Izawa, M. R. M., Cloutis, E. A., Rhind, T., et al. 2019, Icarus, 319, 525
Kitazato, K., Milliken, R., Iwata, T., et al. 2019, Science, 364, 272
Landolt, A. U. 1973, AJ, 78, 959
Landolt, A. U. 1983, AJ, 88, 439
Landolt, A. U. 1992, AJ, 104, 340
Lauretta, D., DellaGiustina, D., Bennett, C., et al. 2019, Nature, 568, 55
Lazzaro, D., Angeli, C. A., Carvano, J. M., et al. 2004, Icarus, 172, 179
Licandro, J., Hargrove, K., Kelley, M., et al. 2012, A&A, 537, A73
Luu, J. X., & Jewitt, D. C. 1990, AJ, 99, 1985
Mainzer, A., Bauer, J., Cutri, R., et al. 2019, NEOWISE Diameters and Albedos V2.0, NASA Planetary Data System
Marsset, M., DeMeo, F. E., Binzel, R. P., et al. 2020, ApJS, 247, 73
Marzari, F., Davis, D., & Vanzani, V. 1995, Icarus, 113, 168
McCord, T. B., & Gaffey, M. J. 1974, Science, 186, 352
McFadden, L. A., Gaffey, M. J., & McCord, T. B. 1984, Icarus, 59, 25
Miller, A. A., Bloom, J. S., Richards, J. W., et al. 2015, ApJ, 798, 122
Morate, D., de León, J., De Prá, M., et al. 2016, A&A, 586, A129
Morate, D., de León, J., De Prá, M., et al. 2018, A&A, 610, A25
Morate, D., de León, J., De Prá, M., et al. 2019, A&A, 630, A141
Mothé-Diniz, T., Roig, F., & Carvano, J. 2005, Icarus, 174, 54
Neckel, H. 1986, A&A, 169, 194
Nesvornỳ, D., Bottke, W. F., Vokrouhlickỳ, D., Morbidelli, A., & Jedicke, R. 2005, Proc. Int. Astron. Union, 1, 289
Nesvorný, D., Brož, M., & Carruba, V. 2015, in Asteroids IV (Tucson: University of Arizona Press), 297
Perna, D., Barucci, M. A., Ishiguro, M., et al. 2017, A&A, 599, L1
Pilorget, C., Okada, T., Hamm, V., et al. 2022, Nat. Astron., 6, 221
Pinilla-Alonso, N., de León, J., Walsh, K., et al. 2016, Icarus, 274, 231
Pinilla-Alonso, N., De Pra, M., de Leon, J., et al. 2021, PRIMASS-L Spectra Bundle V1.0, NASA Planetary Data System, 8
Porto de Mello, G. F., da Silva, R., da Silva, L., & de Nader, R. V. 2014, A&A, 563, A52
Rivkin, A. S., & Emery, J. P. 2010, Nature, 464, 1322
Sarli, B. V., Horikawa, M., Yam, C. H., Kawakatsu, Y., & Yamamoto, T. 2018, J. Astronaut. Sci., 65, 82
Spoto, F., Milani, A., & Knežević, Z. 2015, Icarus, 257, 275
Sugita, S., Honda, R., Morota, T., et al. 2019, Science, 364, eaaw0422
Takir, D., & Emery, J. P. 2012, Icarus, 219, 641
Tatsumi, E., Domingue, D., Schröder, S., et al. 2020, A&A, 639, A83
Tatsumi, E., Popescu, M., Campins, H., et al. 2021a, MNRAS, 508, 2053
Tatsumi, E., Sugimoto, C., Riu, L., et al. 2021b, Nat. Astron., 5, 39
Tedesco, E. F., Tholen, D. J., & Zellner, B. 1982, AJ, 87, 1585
Tholen, D. J. 1984, PhD thesis, University of Arizona, Tucson, USA
Tody, D. 1986, SPIE Conf. Ser., 627, 733
Usui, F., Kasuga, T., Hasegawa, S., et al. 2012, ApJ, 762, 56
Usui, F., Hasegawa, S., Ootsubo, T., & Onaka, T. 2019, PASJ, 71, 1
Vernazza, P., Marsset, M., Beck, P., et al. 2015, ApJ, 806, 204
Vernazza, P., Ferrais, M., Jorda, L., et al. 2021, A&A, 654, A56
Vilas, F. 1994, Icarus, 111, 456
Vilas, F. 2008, AJ, 135, 1101
Walsh, K. J., Delbó, M., Bottke, W. F., Vokrouhlickỳ, D., & Lauretta, D. S. 2013, Icarus, 225, 283
Watanabe, S., Hirabayashi, M., Hirata, N., et al. 2019, Science, 364, 268
Wood, X. H. J., & Kuiper, G. P. 1963, ApJ, 137, 1279
Xiang, M., Ting, Y.-S., Rix, H.-W., et al. 2019, ApJS, 245, 34
Xu, S., Binzel, R. P., Burbine, T. H., & Bus, S. J. 1995, Icarus, 115, 1
Yada, T., Abe, M., Okada, T., et al. 2021, Nat. Astron., 6, 214
Zellner, B., Wisniewski, W. Z., Andersson, L., & Bowell, E. 1975, AJ, 80, 986
Zellner, B., Tholen, D. J., & Tedesco, E. F. 1985, Icarus, 61, 355
Ziffer, J., Campins, H., Licandro, J., et al. 2011, Icarus, 213, 538

Appendix A: Observations of asteroids with the TNG

In this section, we show all the observations presented in this paper made with the TNG telescope. We note that all the asteroid reflectance spectra were derived by dividing the spectra of solar analog Hyades 64. Tables A.1 and A.2 describe the observational conditions and the physical properties of the target asteroids, respectively. The procedure of taxonomic classification is described in Sec. A.1. Figure A.1 shows all the asteroid reflectance spectra presented in this study.

Appendix A.1: ECAS taxonomy

Using the spectrophotometric data obtained by ECAS, based on principal component analysis, Tholen (1984) introduced 12 asteroid spectral types or classes. This taxonomy is so far the only one that takes the NUV region into account. . Tholen (1984) find that especially dark asteroids have a large variation in the NUV and classified them into C, D, T, P, B, F, and G classes. Thus, we classify our spectra based on Tholen's taxonomy.

To classify the asteroids, we computed the discrete spectra through the ECAS filters by convolving the reflectance spectra from the TNG with the transmission curves of the ECAS filters that cover a common wavelength range: u, b, v, and w for the blue part; x and p for the red part. We used the entire spectral range for the classification, in other words, the joined blue (LR-B) and red (LR-R) parts of the spectra. Sometimes, there was a mismatch in the slopes of red and blue parts and they were not able to join. We evaluated the difference in the blue and red slopes computed in the common wavelength region ($0.6 - 0.7\,\mu$m), and if the slope difference was out of the 1.5 interquartile range, we considered them to be outliers. If the red part was not available or if the slope difference was in the outlier range, we proceeded to classify the asteroid using only the blue part of the reflectance spectra.

The next step was to compare this with the reference spectra of the ECAS taxonomy available on the PDS [3]. We used χ^2 to assess the differences between the reference spectra, and the observed asteroid spectra giving three possible taxonomic classes as the first approximation. To discern which taxonomic class was the correct one, we carried out a visual inspection of the spectra, looking for specific features such as the wavelength position of the maximum in reflectance or the presence of absorption bands. We also used the albedo information from the AKARI survey (Usui et al. 2012) to discern between some S (albedo> 0.1) and T (albedo< 0.1) candidates and between E, M, and P candidates. Finally, for those asteroids with χ^2 larger than the χ^2 between taxonomies, very similar χ^2 for different taxonomies, or high dispersion at key wavelengths, such as u and b, we decided to keep all possible taxonomic classes. The results of our classification are shown in the third column of Table A.2. We also show in this table previous taxonomical classifications, when available, from ECAS, SMASS II or S^3OS^2 spectra (based on both the Bus and Tholen taxonomies). The table also includes the asteroid H magnitude, diameter, and albedo (from the AKARI survey), proper orbital elements semimajor axis (a), eccentricity (e), and inclination (i) extracted from the Lowell Minor Planet Service webpage[4], and family membership from Nesvorný et al. (2015) (except for Polana-Eulalia family members, extracted from Walsh et al. 2013). For subsequent compositional analyses (slope computation and comparison to Ryugu and Bennu) we do not use those asteroids that have a rocky or silicate-rich classification (S, Q, A, V, K, R, or L types).

[3] https://sbnarchive.psi.edu/pds3/non_mission/EAR_A_2CP_3_RDR_ECAS_V4_0/data/colorind.tab
[4] https://asteroid.lowell.edu/gui/

Table A.1. Observation conditions

ID	Name	Date and time (UTC)	m_V	Exposure time (s)		Airmass	Phase angle	NUV slope	VIS slope
				LR-B	LR-R		(°)	(μm^{-1})	(μm^{-1})
39	Laetitia	2010-10-31 22:12:52	10.2	60	60	1.33	19.0	2.54 ± 0.01	1.14 ± 0.01
45	Eugenia	2012-02-07 20:18:05	13.3	600	–	1.21	19.2	0.33 ± 0.01	0.28 ± 0.01
47	Aglaja	2012-02-07 04:01:32	13.6	1200	–	1.37	16.9	0.29 ± 0.01	−0.03 ± 0.01
62	Erato	2012-02-06 05:52:21	14.7	1800	–	1.25	14.2	0.30 ± 0.02	−0.44 ± 0.01
82	Alkmene	2010-10-31 21:25:36	13.8	600	600	1.31	15.9	1.38 ± 0.01	0.49 ± 0.01
88	Thisbe	2012-02-07 01:02:52	12.0	600	–	1.18	6.2	−0.00 ± 0.02	−0.13 ± 0.01
96	Aegle	2010-10-31 02:32:40	12.6	300	300	1.06	7.9	1.06 ± 0.01	0.73 ± 0.01
106	Dione	2010-11-11 05:13:06	12.7	300	300	1.0	18.3	1.53 ± 0.02	−0.07 ± 0.01
175	Andromache	2010-10-31 23:05:33	12.0	300	300	1.09	4.3	0.51 ± 0.01	−0.09 ± 0.01
179	Klytaemnestra	2010-11-01 01:54:30	11.8	900	300	1.04	2.5	1.40 ± 0.01	0.80 ± 0.01
207	Hedda	2010-10-31 22:41:44	13.0	300	300	1.12	13.5	0.68 ± 0.02	−0.09 ± 0.01
213	Lilaea	2012-02-08 01:14:42	13.6	1200	–	1.07	5.8	−0.29 ± 0.01	−0.06 ± 0.01
225	Henrietta	2012-02-07 03:08:27	14.9	1200	–	1.36	11.8	0.03 ± 0.02	0.06 ± 0.01
229	Adelinda	2012-02-07 04:45:20	15.1	1800	–	1.17	7.8	0.08 ± 0.02	−0.03 ± 0.01
246	Asporina	2010-10-31 20:39:31	13.5	600	600	1.44	22.3	3.97 ± 0.02	2.27 ± 0.02
261	Prymno	2010-10-31 20:08:41	14.3	600	600	1.51	22.8	0.54 ± 0.01	0.22 ± 0.01
268	Adorea	2012-02-08 06:05:49	13.5	900	–	1.33	21.4	0.41 ± 0.02	0.22 ± 0.01
269	Justitia	2010-11-01 01:06:15	13.6	300	300	1.13	5.1	1.48 ± 0.02	1.65 ± 0.01
314	Rosalia	2012-02-08 02:49:01	16.1	2400	–	1.45	13.7	–	0.12 ± 0.04
379	Huenna	2012-02-08 04:10:59	15.1	1200	–	1.26	13.1	–	0.15 ± 0.01
419	Aurelia	2012-02-08 02:13:13	12.8	900	–	1.17	10.8	0.00 ± 0.02	0.11 ± 0.01
426	Hippo	2012-02-06 21:42:46	13.8	600	–	1.12	19.4	–	0.06 ± 0.01
461	Saskia	2012-02-07 23:37:38	14.4	1200	–	1.25	4.1	0.36 ± 0.02	0.01 ± 0.01
468	Lina	2012-02-06 23:56:46	14.9	1800	–	1.03	9.4	–	0.07 ± 0.02
555	Norma	2012-02-07 02:00:38	15.1	1800	–	1.4	11.7	–	−0.23 ± 0.01
588	Achilles	2010-11-01 04:51:37	14.8	600	600	1.10	7.3	1.13 ± 0.02	0.85 ± 0.01
624	Hector	2010-11-01 06:05:38	14.8	450	450	1.11	8.8	0.75 ± 0.02	1.10 ± 0.01
720	Bohlinia	2010-10-31 05:53:58	14.6	600	600	1.02	17.6	1.50 ± 0.02	0.52 ± 0.02
742	Edisona	2010-10-31 23:34:01	13.5	300	300	1.18	8.1	1.53 ± 0.02	0.73 ± 0.01
747	Winchester	2012-02-08 04:54:39	13.8	1800	–	1.07	14.1	0.52 ± 0.02	0.34 ± 0.01
808	Merxia	2010-10-30 22:03:32	14.5	600	600	1.26	17.8	1.92 ± 0.02	0.79 ± 0.01
919	Ilsebill	2010-10-30 22:46:27	15.5	600	–	1.10	14.7	1.01 ± 0.02	0.10 ± 0.01
936	Kunigunde	2012-02-08 00:19:54	15.7	1800	–	1.04	1.9	–	−0.21 ± 0.01
954	Li	2012-02-07 21:41:30	16.1	1800	–	1.15	16.8	–	0.14 ± 0.01
1126	Otero	2010-11-01 03:36:51	14.9	600	–	1.04	11.7	2.34 ± 0.02	1.15 ± 0.01
1214	Richilde	2010-10-31 19:27:34	15.9	600	600	1.26	24.3	0.59 ± 0.02	0.29 ± 0.01
1471	Tornio	2010-10-31 02:58:04	14.7	600	600	1.04	13.6	0.19 ± 0.02	0.68 ± 0.01
1534	Nasi	2010-11-12 06:04:53	15.4	720	720	1.01	25.6	1.30 ± 0.02	0.08 ± 0.01
1662	Hoffmann	2010-11-13 05:44:23	16.0	1200	1200	1.01	20.7	1.81 ± 0.02	0.86 ± 0.02
1904	Massevitch	2010-10-31 03:32:21	15.0	600	600	1.14	10.1	1.50 ± 0.01	0.63 ± 0.02
1929	Kollaa	2010-11-01 03:04:11	15.6	600	600	1.27	2.9	2.04 ± 0.02	0.84 ± 0.02
2026	Cottrell	2010-11-12 21:12:20	17.7	1800	1800	1.15	2.5	–	0.08 ± 0.02
2354	Lavrov	2010-11-01 00:36:53	15.2	600	600	1.09	5.9	1.86 ± 0.02	0.91 ± 0.01
2715	Mielikki	2010-10-30 21:19:11	15.3	900	900	1.18	19.5	2.09 ± 0.02	1.03 ± 0.01
3451	Mentor	2010-10-30 20:22:18	16.0	1200	900	1.26	12.1	0.68 ± 0.02	0.32 ± 0.01
3485	Barucci	2010-10-31 00:00:18	16.2	600	600	1.10	10.3	0.01 ± 0.02	0.01 ± 0.01
3667	Anne-Marie	2010-11-10 21:38:43	18.9	1200	1200	1.73	11.4	–	−0.16 ± 0.02
5142	Okutama	2010-10-30 23:21:32	14.9	600	600	1.1	14.4	1.58 ± 0.02	0.68 ± 0.01
5158	Ogarev	2010-11-13 04:25:55	17.3	1800	1800	1.06	14.9	0.05 ± 0.03	−0.01 ± 0.01
5924	Teruo	2010-11-12 22:36:08	17.3	1800	1800	1.13	12.2	−0.12 ± 0.02	0.00 ± 0.01
6142	Tantawi	2010-11-11 01:18:21	17.5	1500	1500	1.06	2.4	−0.55 ± 0.03	−0.26 ± 0.02
6578	Zapesotskij	2010-11-10 22:49:23	17.3	1200	1200	1.21	21	0.07 ± 0.03	−0.04 ± 0.01
6661	Ikemura	2010-10-31 05:24:34	16.5	600	600	1.10	19.1	−0.30 ± 0.02	−0.09 ± 0.01
6698	Malhotra	2010-10-31 01:13:51	16.5	600	600	1.15	7.8	−0.03 ± 0.03	−0.06 ± 0.02
		2010-11-11 23:23:54	16.6	1200	1200	1.07	4.9	−0.09 ± 0.02	−0.08 ± 0.01
6769	Brokoff	2010-11-11 04:04:25	17.3	1150	1200	1.01	22.1	−0.38 ± 0.03	0.02 ± 0.02
6815	Mutchler	2010-11-12 03:06:33	17.4	1800	–	1.02	13.4	1.57 ± 0.02	0.45 ± 0.02
6840	1995WW5	2010-11-11 22:07:35	17.4	1600	1800	1.15	16.7	−0.06 ± 0.03	−0.10 ± 0.01
7081	Ludibunda	2010-11-01 00:06:14	15.3	600	600	1.03	4.8	1.81 ± 0.02	0.94 ± 0.01
8424	Toshitsumita	2010-10-31 00:37:44	16.0	600	600	1.13	9.2	0.45 ± 0.02	0.19 ± 0.01
9052	Uhland	2010-11-11 20:45:59	17.2	1800	1800	1.13	21.5	−0.07 ± 0.02	−0.11 ± 0.01
13100	1993FB10	2010-10-31 04:27:42	17.2	900	900	1.09	14.9	1.80 ± 0.03	0.85 ± 0.02
		2010-11-13 03:18:21	16.9	1500	1500	1.09	8.1	2.29 ± 0.02	1.01 ± 0.02
14112	1998QZ25	2010-11-11 02:45:01	16.9	1200	–	1.00	11.5	1.62 ± 0.03	0.73 ± 0.03
25490	Kevinkelly	2010-11-10 23:58:17	17.3	1500	1500	1.03	6.8	−0.10 ± 0.03	−0.03 ± 0.01
33804	1999WL4	2010-11-13 01:35:05	17.1	1800	1800	1.04	3.3	0.47 ± 0.02	0.04 ± 0.01
43962	1997EX13	2010-11-13 00:10:23	17.1	1800	–	1.01	2.5	1.60 ± 0.03	0.57 ± 0.02
49833	1999XB84	2010-11-12 00:45:31	17.7	1800	1800	1.07	4.9	0.11 ± 0.03	−0.09 ± 0.01
219071	1997US9	2010-11-01 04:20:37	16.5	600	600	1.25	17.8	2.32 ± 0.7	0.81 ± 0.03

Table A.2. Physical information of target asteroids, including taxonomical classification, albedo, diameter, proper orbital elements (*a*, *e*, and *i*), absolute magnitude (H), and family membership. Family names with "()" indicate possible misclassifications (see Sec. 4.2).

ID	Name	Taxonomy (This study)	Taxonomy Bus	Taxonomy Tholen	Albedo	Diameter (km)	a (au)	e	i (°)	H	Family
39	Laetitia	S/A	S	S	0.282±0.008	152±2	2.77	0.112	10.4	6.10	
45	Eugenia	P/C†	C	FC	0.056±0.002	184±4	2.71	0.084	6.6	7.46	
47	Aglaja	B†	C	B	0.060±0.004	147±2	2.88	0.130	4.0	7.84	
62	Erato	B†	Ch	BU	0.091±0.002	79±1	3.13	0.168	2.2	8.76	Themis
82	Alkmene	Q/S	Sq	S	0.19±0.005	64±1	2.76	0.220	2.8	8.40	
88	Thisbe	B†	B	CF	0.071±0.002	196 ±3	2.77	0.162	5.2	7.04	
96	Aegle	T	T	T	0.056±0.002	165±3	3.05	0.141	16.0	7.67	Aegle
106	Dione	G	Cgh	G	0.084±0.003	153±2	3.18	0.159	4.6	7.41	
175	Andromache	C/B	Cg	C	0.093±0.004	96±2	3.19	0.233	3.2	8.31	
179	Klytaemnestra	S	Sk	S	0.245±0.007	64±1	2.97	0.110	7.8	8.15	
207	Hedda	C	Ch	C	0.047±0.002	64±1	2.28	0.030	3.8	9.92	
213	Lilaea	F†	B	F	0.107±0.003	76±1	2.75	0.144	6.8	8.64	
225	Henrietta	B/F/C†	–	F	0.051±0.002	108 ±2	3.39	0.263	20.9	8.72	
229	Adelinda	B/F†	Cb*	BCU	0.034±0.001	109±1	3.43	0.139	2.1	9.13	
246	Asporina	A/S[1]	A	A	0.177±0.005	60±1	2.69	0.109	15.6	8.62	
261	Prymno	C/M	X	B	0.149±0.004	44.7±0.5	2.33	0.089	3.6	9.44	
268	Adorea	P/C†	X*	FC	0.046±0.001	136±2	3.09	0.137	2.4	8.28	Themis
269	Justitia	D[1]	Ld	–	0.082±0.002	59±1	2.62	0.213	5.5	9.50	
314	Rosalia	C/G†	B*	B*	0.087±0.003	57±1	3.16	0.171	12.5	9.50	
379	Huenna	C†	C	B	0.075±0.002	82±1	3.14	0.180	1.7	8.87	Themis
419	Aurelia	F†	Cb	F	0.051±0.002	122±2	2.60	0.251	3.93	8.42	
426	Hippo	C/B/G/F†	X*	F	0.052±0.002	121±2	2.89	0.106	19.5	8.42	
461	Saskia	C/B†	X	FCX	0.069±0.005	43±1	3.12	0.144	1.5	10.5	Themis
468	Lina	C/B/G/F†	Xk*	DPF	0.059±0.002	60± 1	2.52	0.197	21.4	9.83	Themis
555	Norma	B/F†	B	–	0.101±0.004	32±1	3.19	0.152	2.7	10.6	Themis
588	Achilles	T	–	DU	0.035±0.002	133±3	5.21	0.147	10.3	8.67	
624	Hector	D	–	D	0.034±0.001	231±4	5.26	0.023	18.2	7.49	Hector
720	Bohlinia	S/Q	Sq	S	0.199±0.007	34 ± 0.5	2.89	0.186	2.4	9.71	Koronis
742	Edisona	S	K	S	0.122±0.004	47.3±0.6	3.01	0.116	11.2	9.55	Eos
747	Winchester	P/C†	C	PC	0.052±0.002	170± 3	3.00	0.339	18.2	7.69	
808	Merxia	S	S	Sq	0.206±0.006	34±0.4	2.75	0.129	4.7	9.70	Merxia
919	Ilsebill	C/G†	C	–	0.048±0.002	33±0.5	2.77	0.084	8.2	11.3	
936	Kunigunde	B/F†	B*	B*	0.124±0.007	38±1	3.13	0.176	2.4	10.0	Themis
954	Li	C/G†	Cb*	FCX	0.068±0.002	53±1	3.13	0.174	1.2	9.94	Themis
1126	Otero	A/S†	A	–	0.399± 0.32[#]	11.0±0.9[#]	2.27	0.148	6.5	11.9	
1214	Richilde	P	Xk	–	0.064±0.002	34.9±0.5	2.71	0.117	9.8	10.9	
1471	Tornio	P	T	–	0.052±0.002	42±0.6	2.72	0.119	13.6	10.7	
1534	Nasi	G	Cgh	–	0.100±0.004	19.5 ±0.4	2.73	0.252	9.8	11.7	Chloris
1662	Hoffmann	S	Sr	–	0.258±0.108[#]	12.4 ± 2.7[#]	2.74	0.173	4.23	11.6	Merxia
1904	Massevitch	R	R	R*	0.581±0.228[#]	13.5 ± 0.2[#]	2.74	0.073	12.8	11.2	
1929	Kollaa	R	V	–	0.393±0.066[#]	6.7±0.3[#]	2.36	0.075	7.8	12.7	Vesta
2026	Cottrell	C/P/F	–	–	0.088±0.009	13.2 ±0.6	2.45	0.115	2.5	12.8	New Polana
2354	Lavrov	S	L	–	0.154±0.022	14.9±1.0	2.73	0.104	3.3	11.8	Henan
2715	Mielikki	S	A	–	0.136±0.017	15.1 ±0.9	2.74	0.150	6.7	11.9	
3451	Mentor	P	X	–	0.075 ±0.005	118±3	5.15	0.071	24.6	8.10	
3485	Barucci	F	–	–	0.075±0.003	14.7 ±0.3	2.44	0.166	1.8	12.6	New Polana
3667	Anne-Marie	F	–	–	0.064 ±0.003	23.2 ±0.5	3.08	0.231	16.2	11.8	Tirela
5142	Okutama	S/Q	Sq	–	0.632 ±0.097	7.3±0.5	2.54	0.277	6.3	11.8	
5158	Ogarev	F	–	–	0.067 ±0.012	7.8 ± 0.7	2.42	0.179	3.1	14.1	New Polana
5924	Teruo	F	–	–	0.054 ±0.004	14.8±0.5	2.35	0.110	4.1	13.0	Polana-Eulalia
6142	Tantawi	F	–	–	0.092± 0.034[#]	9.2± 1.7[#]	2.46	0.138	2.9	13.7	Eulalia
6578	Zapesotskij	F	–	–	0.061 ± 0.005[#]	7.9± 0.1[#]	2.42	0.189	3.6	14.5	New Polana
6661	Ikemura	F	–	–	0.087 ±0.004	10.9±0.2	2.38	0.172	2.7	13.2	New Polana
6698	Malhotra	F	–	–	0.097 ±0.011	8.3±0.5	2.44	0.168	2.5	13.6	Eulalia
6769	Brokoff	F	–	–	0.052 ±0.006	12.8±0.7	2.42	0.123	3.9	13.3	New Polana
6815	Mutchler	Q/S†	–	–	–	–	2.43	0.192	1.6	14.7	Nysa
6840	1995WW5	F	–	–	0.043±0.008[#]	8.6 ±0.1[#]	2.43	0.153	3.4	14.5	Eulalia
7081	Ludibunda	S	K	–	0.143 ± 0.010[#]	10.1±0.1[#]	2.75	0.239	6.7	12.9	Nysa
8424	Toshitsumita	C	–	–	0.165±0.03[#]	5.2 ± 0.1[#]	2.40	0.196	3.7	13.9	(New Polana)
9052	Uhland	F	–	–	0.047± 0.004	10.2±0.4	2.46	0.186	2.2	13.9	Eulalia
13100	1993FB10	S	–	–	–	–	2.44	0.193	3.5	14.4	Nysa
14112	1998QZ25	S†	–	–	0.220±0.104[#]	4.3 ± 0.8	2.46	0.161	2.8	14.4	(Eulalia)
25490	Kevinkelly	B	–	–	0.043±0.007	8.1±0.7	2.43	0.149	2.0	14.5	Eulalia
33804	1999WL4	C	–	–	0.072±0.011[#]	5.4±0.1[#]	2.40	0.141	3.7	15.0	New Polana
43962	1997EX13	S/Q†	–	–	0.171±0.020[#]	2.8±0.1[#]	2.38	0.159	2.1	15.3	(New Polana)
49833	1999XB84	F	–	–	0.064±0.004[#]	4.3±0.1[#]	2.42	0.168	4.0	15.8	Eulalia
219071	1997US9	S	Q	–	0.383±0.220[#]	0.7 ±0.2	1.05	0.282	20.0	17.1	

Notes. [(*)] Spectra from S^3OS^2(Lazzaro et al. 2004). [(#)] Albedo and/or diameter values from NEOWISE survey (Mainzer et al. 2019). [(†)] Classification only using blue spectrum (LR-B). [(1)] Unusually red slope.

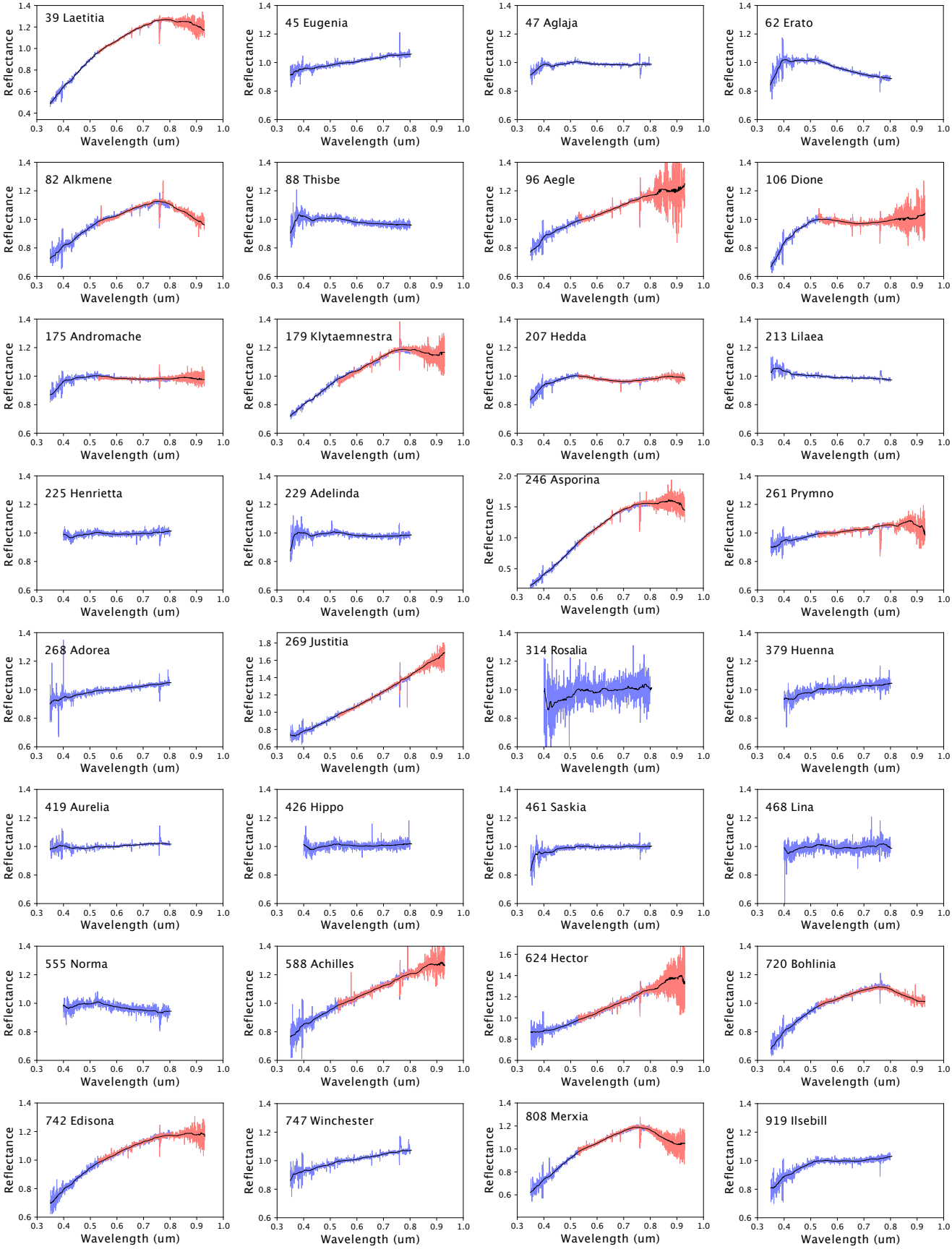

Fig. A.1. Asteroid reflectance spectra normalized to unity at 0.55 μm. Blue and red lines show the original spectra obtained with LR-B (blue) and LR-R (red) grisms, respectively. Black lines correspond to the smoothed spectra obtained by running a median filter using a window of ~ 30 nm and plotted for the sake of better visualization.

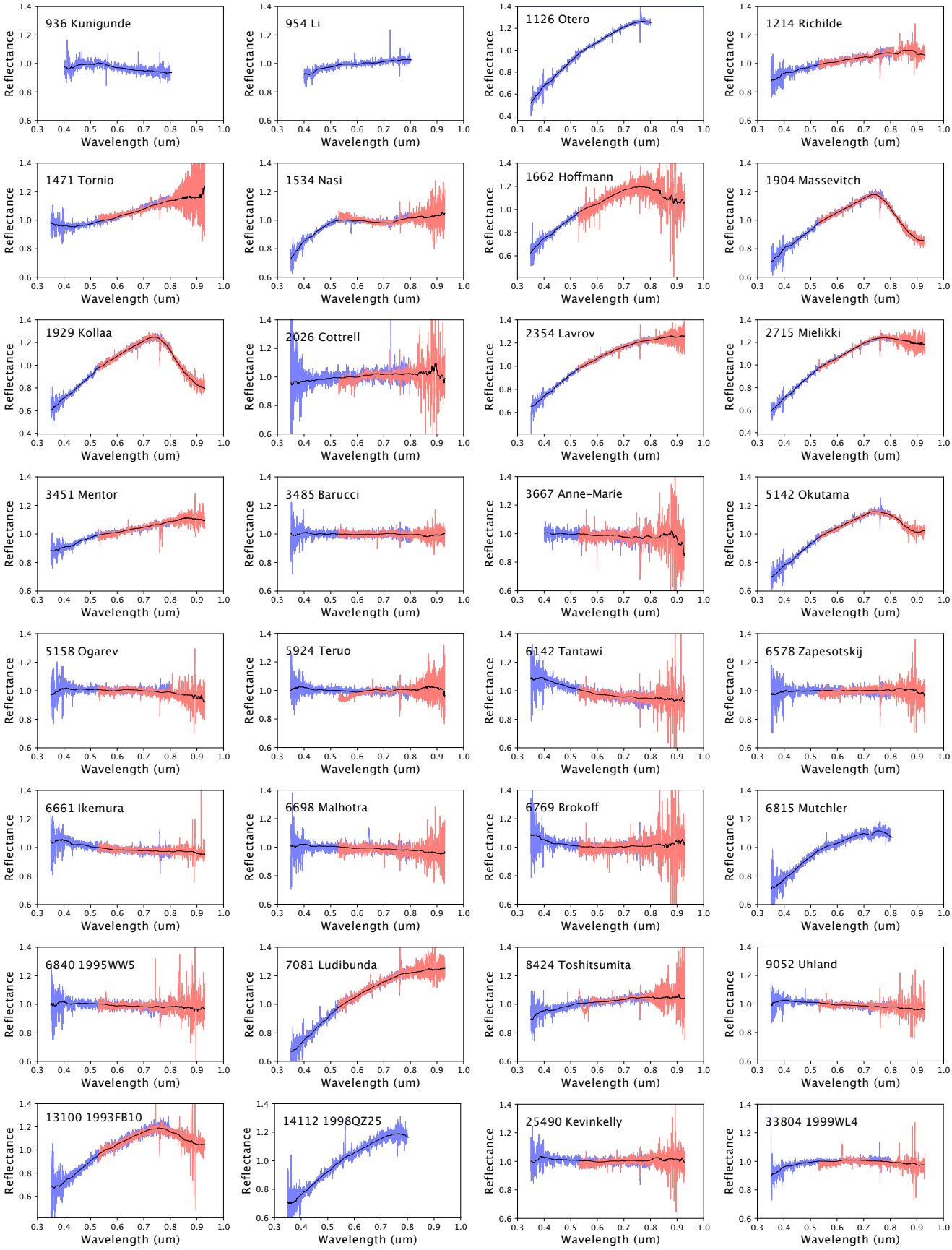

Fig. A.1. continued.

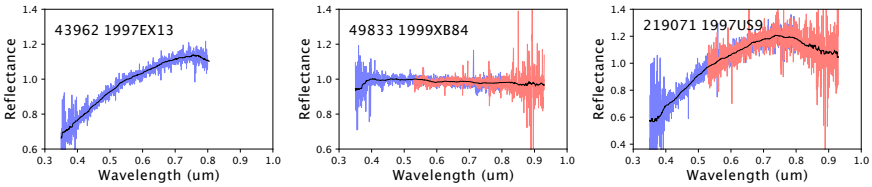

Fig. A.1. continued.